Trajectory Optimisation under Uncertainties

Final Report

Authors: F. Bernelli-Zazzera, M. Lavagna, R. Armellin, P. Di Lizia, A. Morselli
Affiliation: Department of Aerospace Engineering, Politecnico di Milano

ACT Researchers: J. Olympio, D. Izzo

Date: 01/10/2012

Contacts:

Franco Bernelli-Zazzera
Tel: +39-02-23998328
Fax: +39-02-23998334
e-mail: franco.bernelli@polimi.it

Leopold Summerer (Technical Officer)
Tel: +31(0)715654192
Fax: +31(0)715658018
e-mail: act@esa.int

Available on the ACT website
http://www.esa.int/act

Ariadna ID: 10/4101
Ariadna study type: Standard
Contract Number: 4000103161

Contents

List of Figures

List of Tables

Abstract

The early stage of space trajectory design assumes that the dynamics modelling exactly represents the reality. Unfortunately, the accuracy of the dynamical models is affected by perturbations and the knowledge of systems configuration is limited during the first phases of space mission design. In addition, several space-related applications involve the identification of trajectories with uncertain constraints and terminal conditions. The designer is then asked to deal with uncertainties, which cannot be fully removed. Classical methods for uncertainty management are based on linear approximations, whose accuracy drops off rapidly in highly nonlinear dynamics. Thus, several nonlinear strategies have recently appeared to overcome this issue.

This work focuses on the design of transfer trajectories for continuously propelled spacecraft and on the development of an optimal nonlinear control strategy to manage uncertain boundary conditions. A high order optimal control strategy is proposed, based on the use of differential algebraic techniques. In the frame of orbital mechanics, differential algebra is used to represent, by high order Taylor polynomials, the dependency of the spacecraft state on initial conditions and environmental parameters. The resulting polynomials are manipulated to obtain the high order expansion of the solution of fuel-optimal control problems about reference trajectories, including constraints on control saturation. Whenever perturbations in the nominal conditions occur, new optimal control laws for perturbed initial and final states are obtained by the mere evaluation of polynomials. Illustrative applications are presented in the frame of the optimal low-thrust transfer to asteroid 1996 FG_3.

Key words: Space trajectory design; Optimal control; Low-thrust transfers; Saturating actuators; Uncertainty management; High order methods

Chapter 1

Introduction

Space trajectories are usually designed by solving optimal control problems in nominal conditions; i.e., at the design stage, the dynamics modelling is supposed to exactly represent the reality [20]. Unfortunately, the accuracy of the dynamical models is affected by the representation of all the possible perturbations. The problem is however that their accurate description is difficult to produce, especially during the design phase. The designer is then asked to deal with uncertainties, which cannot be fully removed.

Uncertainty does not owe to dynamics perturbations only. The limited knowledge of the system configuration during the first phases of space mission design introduces significant uncertainty in the space system as well (e.g., spacecrafts mass and size, thrusters performances). Systems properties are parameters of the adopted mathematical model and are affected by given levels of uncertainty. In addition, several space-related applications involve the solution of optimal control problems with both uncertain constraints and terminal conditions. A typical example is the problem of targeting an asteroid (e.g., during a deflection mission). The orbital parameters of the asteroid are known only to a given precision and, thus, its position and velocity are accurately identified quite late in real scenarios.

In the light of the above observations, it is clear that mission analysts cannot ignore the presence of uncertainty during the design process. The optimal control problems must then be posed using explicit uncertainties either in the dynamics or in the constraints. This is evident if one considers the drastic effects that uncertainties might have on the achievement of the mission goals if not properly managed. The deviation of the spacecraft trajectory from its nominal path due to unmodelled perturbations or uncertain parameters increases very rapidly with time due to errors accumulation. Effective algorithms exist to correct the spacecraft path with impulsive maneuvers. However, the recent advances in low-thrust propulsion systems

strongly encourage the future design of interplanetary low-thrust missions, which show the appealing feature of saving a significant amount of propellant with respect to the classical chemical solution. On the other hand, low-thrust propulsion systems provide very small thrust acceleration. This yields two main consequences, which strongly affect mission operations. First of all, the total thrust duration necessary to transfer the spacecraft from its initial state to the trajectory is significantly larger than the typical need of a chemical propulsion system. Consequently, the risk of accumulation of uncertainties along the trajectory is extremely high. Moreover, even though low-thrust propulsion systems allow correction maneuvers to have small mass impact for wide discrepancies between the flown trajectory and the nominal one, more time to complete such maneuvers is required. Going to extremes, the issue might be that there may not be sufficient time to perform them.

Effective and innovative strategies must be developed to deal with these new problems posed by the increasing use of continuously propelled trajectories. Such strategies must be able to embed the management of uncertainties directly into the solution of the optimal control problems. More specifically, as developing and using accurate dynamical models during the design phase is not an easy task, the new methods should allow the designer to use mid-fidelity dynamical models, and to include unmodelled disturbances as uncertain, bounded terms. In this way, all uncertainties are taken into account during the design process, ensuring the assessment of the proper mission margins. Thus, even if the spacecraft flies far from the designed trajectory in real scenarios, it will always have enough propellant and time to perform the corrections, as far as the actual physical perturbations lie within the considered ranges.

The problem of computing optimal control trajectories in low-thrust dynamics with uncertain boundary conditions is addressed in this work. The problem of transferring a spacecraft from an initial state $\boldsymbol{x}_i$ to a finale state $\boldsymbol{x}_f$ under the general dynamics

$$\dot{\boldsymbol{x}} = \boldsymbol{f}(\boldsymbol{x}, \boldsymbol{T}, t), \tag{1.1}$$

is considered, where $\boldsymbol{T}$ is the thrust vector. The optimal control problem aims at finding the thrust profile $\boldsymbol{T}(t)$ that minimizes fuel consumption. The initial and final spacecraft states are supposed to be affected by uncertainties, $\boldsymbol{x}_i + \delta\boldsymbol{x}_i$ and $\boldsymbol{x}_f + \delta\boldsymbol{x}_f$ respectively. The aim of this work is to provide mission analysts with an effective tool for the fast and optimal correction of the the thrust profile to compensate such uncertainties, including system nonlinearities and path constraints for actuators saturation, $T(t) = \|\boldsymbol{T}(t)\| \leq T_{\max}$, $\forall\, t$.

Many techniques have been developed in the past to deal with the previous problem. They can be stochastic or non-stochastic methods, depending on the approach adopted to represent and deal with the uncertainties.

In a stochastic formulation, uncertainty is introduced through statistics, which can either represent possible values of uncertain parameters or describe unknown dynamics by means of Brownian noise and Wiener processes [17]. Indirect methods and stochastic dynamic programming techniques are then used to solve the resulting optimal control problem [23, 35, 36].

Non-stochastic approaches make no assumptions about the probability associated to parameters and outcomes. Any uncertainty is represented by either discrete or continuous sets of values of equal probability. Techniques belonging to this group range from straight scenario analysis to min-max or information-gap theory approaches. In the first one, a large series of cases, issuing from unknown facets of the problem at hand, are simulated and used to make a final decision; in the latter the maximization of a performance index is sought, while minimizing deviations on the outcome due to uncertainties. The relatively simple approach of scenario analysis has the main drawback of becoming computationally prohibitive as the number of uncertain parameters grows, due to the steep increase of scenarios to be simulated. On the other hand, one of the main issues of the min-max approach is the computation of the deviation of the outcome. Various techniques have been developed in the past to solve this issue, such as interval analysis [29].

The main idea beneath interval analysis is the substitution of real numbers with intervals of real numbers. Interval arithmetic and analysis are then developed to operate on the set of interval numbers in place of the classical analysis of real numbers. Consequently, by performing all operations on an interval input that contains the set of all its possible values, the output interval will consist of all possible values of the result. This turns out to be an effective tool for error and uncertainty propagation, as both numerical errors and uncertainties can be bounded by means of intervals. Unfortunately, the naïve application of interval analysis might result in an artificial and unacceptable overestimation of the solution set when intervals are to be propagated along a trajectory through the integration of a set of ordinary differential equations. The reasons for such an overestimation are the so-called dependency problem and wrapping effect [4].

Semi-analytic techniques and high order methods have recently gained particular interest as alternatives to interval analysis and classical first order methods. The design of optimal control laws to compensate uncertainties was originally developed for linear systems. In linear optimal control theory, the system is assumed linear and the feedback controller is constrained to be linear with respect to its input [15]. First order methods have been deeply

used in the past [18] in many engineering fields, and control strategies to overcome possible navigation errors based on first order expansions of the dynamics are extensively used in spaceflight mechanics [25]. However, the technological challenges imposed by the recent advances in aerospace engineering are demanding stringent accuracy requirements and cost reduction for the control of nonlinear systems. Unfortunately, the accuracy of linearized dynamics can drop off rapidly in nonlinear aerospace applications, affecting the performances of linear optimal controller. Thus, nonlinear optimal feedback control theory has gained interest in the past decades.

Various aspects of nonlinear optimal control have been addressed. Several techniques are available for solving control-affine problems, which are mainly based on dynamic programming or calculus of variations. In Bellmans dynamic programming, the problem is approached by reducing it to solving the nonlinear first-order partial differential Hamilton-Jacobi-Bellman (HJB) equation [13]. The solution to the HJB equation determines the optimal feedback control, but its use is very intricate in practical problems. An alternative approach is based on the calculus of variations and Pontryagins maximum principle, which show the Hamiltonian nature of the second order information of the optimal control problem [12]. Within this frame, the problem is reduced to a two-point boundary value problem (TPBVP) that is solved, in general, by successive approximation of the optimal control input using iterative numerical techniques. However, the solution determined is only valid for one set of boundary conditions, which prevents its immediate use for feedback control.

The complexity of finding the exact solution of the HJB equation has motivated research for approximated methods that are able to supply suboptimal laws for the closed-loop control of nonlinear systems. The State-dependent Riccati equation (SDRE) control method is among the more attractive tools to obtain such approximate solutions. It was originally proposed by Pearson [34], and Wernli and Cook [37], and then described in details by Mracek and Cloutier [30], and Beeler [3]. This method involves manipulating the governing dynamic equations into a pseudo-linear non-unique form in which system matrices are given as a function of the current state and minimizing a quadratic-like performance index. An algebraic Riccati equation using the system matrices is then solved repetitively online to give the optimal control law. Thus, the SDRE approach might turn out to be computationally expensive when the solution of the Riccati equation is not properly managed. This can prevent its use for real-time optimal control. A significant computational advantage can be obtained with the $\theta - D$ technique [38]. Similarly to SDRE, the $\theta - D$ technique relies on an approximate solution to the HJB equation. However, it offers a great computational ad-

vantage for onboard implementation without solving the Riccati equation repetitively at every instant.

Recent advances have been made in the frame of variational approach to optimal control theory. Second order methods were introduced by Bullock [14] and then extended by Olympio [31] to space trajectory design. Based on the Hamiltonian nature of the optimal control problem, the method computes a linear control update iteratively using the gradient of the Hamiltonian function. A higher order approach was introduced by Park and Scheeres [33] through the theory of canonical transformations. More specifically, canonical transformations solve boundary value problems between Hamiltonian coordinates and momenta for a single flow field. Thus, based on the reduction of the optimal control problem to an equivalent boundary value problem, they can be effectively used to solve the optimal control problem analytically as a function of the boundary conditions, which is instrumental to optimal feedback control. The main difficulty of this approach is finding the generating functions via the solution of the Hamilton-Jacobi equation. This problem was solved by Park and Scheeres by expanding the generating function in power series of its arguments.

Limited research has been devoted to develop efficient nonlinear techniques handling control saturation. The introduction of control bounds in the SDRE approach was addressed by Mracek and Cloutier [30, 16]. More specifically, they transformed the nonlinear regulator problem with bounded control into a near-equivalent problem with the form of a nonlinear regulator problem to avoid singularities. A solution procedure was introduced by Park and Scheeres for the generating function method to accommodate control constraints, which is based on the fact that the optimal cost function can be related to the generating functions even in presence of control bounds [32].

A high order method based on the use of differential algebraic techniques is proposed in this work. Differential algebra (DA) serves the purpose of computing the derivatives of functions in a computer environment. More specifically, by substituting the classical implementation of real algebra with the implementation of a new algebra of Taylor polynomials, it expands any function f of v variables into its Taylor series up to an arbitrary order n [6, 11]. The analytical information available with a DA based computation can be used during space trajectory design. As an example, consider the optimal control of space trajectories. Using differential algebra yields the embedded possibility of approximating the dependency of the final spacecraft state on initial conditions, environmental, and control parameters by means of high order Taylor series expansions. Taylor series can then be processed to explicitly solve either the mission constraints or the optimality conditions. This leads to the possibility of designing optimal corrections of

the nominal control to achieve the mission goals. The control strategy is eventually reduced to a simple polynomial evaluation, which is particularly suited for application on on-board autonomous software.

The high order expansions of both the flow of ODE and the solution of parametric implicit equations has already enabled the development of algorithms for astrodynamics applications, such as:

- the robust guidance of interplanetary trajectories applied to a low-thrust Earth-Mars transfer with uncertain departure epoch and to an aerocapture at Mars with uncertain density model, aerodynamic coefficients, and entry flight path angle [20];
- the high order expansion of the solution of two-point boundary value problems (TPBVP) in astrodynamics applied to the computation of families of halo orbits in the restricted circular three-body problem and aerocapture trajectories at Mars [21];
- the characterization of Apophis close encounter with the Earth considering uncertain initial conditions derived from the orbit determination process [1].

In addition, following the reduction of the optimal control problem to a TPBVP, DA techniques have been shown to enable the expansion of the OCP solution about a reference trajectory with respect to either initial or terminal conditions [22]. The computation of feedback control laws in relatively large neighborhoods of the reference trajectory is then reduced to the mere evaluation of high order polynomials. The present study introduces the management of saturation constraints in the DA framework to define an high order optimal feedback control algorithm with saturating actuators. The control constraints are included in the OCP formulation and a minimum fuel mass low-thrust transfer problem is solved. A DA-based algorithm to compute arbitrary order expansions of the associated optimal solution about reference trajectories with respect to initial and terminal conditions is presented. The computation of both optimal thrust direction and switching times for displaced initial spacecraft and final target states is again reduced to the mere evaluation of high order polynomials.

The report is organized as follows. Differential algebra is introduced in Chapter 2, where its application to the high order expansion of ODE flow is presented. Chapter 3 is devoted to illustrate the fuel-optimal interplanetary low-thrust transfer problem; in addition, an innovative smoothing method to identify nominal solutions to the optimal control problem is presented and its performances are assessed on a transfer to asteroid 1996 FG_3. Two DA-based high order algorithms to manage uncertain boundary conditions are

presented in Chapter 4 and Chapter 5. More specifically, smoothing is applied in Chapter 4 to avoid dealing with discontinuous control profiles, whereas a method to handle the exact bang-bang control structure is presented in Chapter 5. In both cases, the performances of the methods are assessed on the transfer to asteroid 1996 FG_3 for various transfer times and switching structures. Chapter 6 concludes the paper and provides hints for future developments.

Chapter 2

Notes on Differential Algebra and Taylor Models

In this chapter the tools used to perform the analysis are presented. Some notes on the theory of differential algebra and Taylor models are given together with their application to the integration of systems of ODE.

2.1 Notes on Differential Algebra

DA techniques find their origin in the attempt to solve analytical problems by an algebraic approach [6]. Historically, the treatment of functions in numerics has been based on the treatment of numbers, and the classical numerical algorithms are based on the mere evaluation of functions at specific points. DA techniques rely on the observation that it is possible to extract more information on a function rather than its mere values. The basic idea is to bring the treatment of functions and the operations on them to the computer environment in a similar way as the treatment of real numbers. Referring to Fig. 2.1, consider two real numbers a and b. Their transformation into the floating point representation, $\overline{a}$ and $\overline{b}$ respectively, is performed to operate on them in a computer environment. Then, given any operation $\times$ in the set of real numbers, an adjoint operation $\otimes$ is defined in the set of floating point (FP) numbers such that the diagram in Figure commutes[1]. Consequently, transforming the real numbers a and b into their FP representation and operating on them in the set of FP numbers return the same result as carrying out the operation in the set of real numbers and then transforming the achieved result in its FP representation. In a similar way, suppose two sufficiently regular functions f and g are given. In the framework of differential algebra,

[1]The diagram commutes approximately in practice, due to truncation errors.

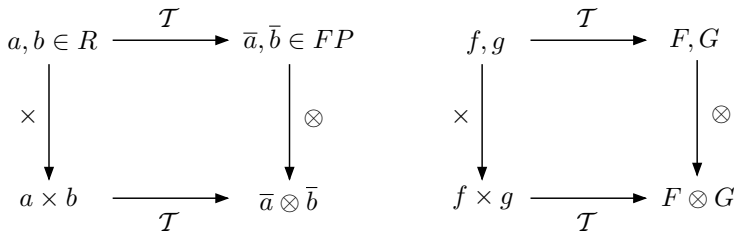

Figure 2.1: Analogy between the floating point representation of real numbers in a computer environment (left figure) and the introduction of the algebra of Taylor polynomials in the differential algebraic framework (right figure).

the computer operates on them using their Taylor series expansions, F and G respectively. Therefore, the transformation of real numbers in their FP representation is now substituted by the extraction of the Taylor expansions of f and g. For each operation in the space of sufficiently continuous functions, an adjoint operation in the space of Taylor polynomials is defined such that the corresponding diagram commutes; i.e., extracting the Taylor expansions of f and g and operating on them in the function space returns the same result as operating on f and g in the original space and then extracting the Taylor expansion of the resulting function. The straightforward implementation of differential algebra in a computer allows to compute the Taylor coefficients of a function up to a specified order n, along with the function evaluation, with a fixed amount of effort. The Taylor coefficients of order n for sums and product of functions, as well as scalar products with reals, can be computed from those of summands and factors; therefore, the set of equivalence classes of functions can be endowed with well-defined operations, leading to the so-called truncated power series algebra [7, 8].

Similarly to the algorithms for floating point arithmetic, the algorithm for functions followed, including methods to perform composition of functions, to invert them, to solve nonlinear systems explicitly, and to treat common elementary functions [9, 6]. In addition to these algebraic operations, also the analytic operations of differentiation and integration are introduced, so finalizing the definition of the DA structure. The differential algebra sketched in this section was implemented by M. Berz and K. Makino in the software COSY-Infinity [11].

2.2 High Order Expansion of the Flow

The differential algebra introduced in the previous section allows the derivatives of any function f of v variables to be computed up to an arbitrary order n, along with the function evaluation. This has an important consequence when the numerical integration of an ODE is performed by means of an arbitrary integration scheme. Any explicit integration scheme is based on algebraic operations, involving the evaluations of the ODE right hand side at several integration points. Therefore, carrying out all the evaluations in the DA framework allows differential algebra to compute the arbitrary order expansion of the flow of a general ODE initial value problem.

Without loss of generality, consider the scalar initial value problem

$$\begin{cases} \dot{x} = f(x,t) \\ x(t_i) = x_i. \end{cases} \tag{2.1}$$

Replace the point initial condition x_i with the DA representative of its identity function; i.e., consider the perturbed initial condition $[x_i] = x_i + \delta x_i$. If all the operations of the numerical integration scheme are carried out in the framework of differential algebra, the Taylor expansion of the solution with respect to the initial condition is obtained at each step. As an example, consider the forward Euler's scheme

$$x_k = x_{k-1} + \Delta t \cdot f(x_{k-1}) \tag{2.2}$$

and analyze the first integration step, i.e.,

$$x_1 = x_0 + \Delta t \cdot f(x_0), \tag{2.3}$$

where $x_0 = x_i$. Substitute the initial value with $[x_0] = [x_i] = x_i^0 + \delta x_i$ in (2.3) for

$$[x_1] = [x_0] + \Delta t \cdot f([x_0]). \tag{2.4}$$

If the function f is evaluated in the DA framework, the output of the first step, $[x_1]$, is the Taylor expansion of the solution x_1 at t_1 with respect to the initial condition about the reference point x_i^0. The previous procedure can be inferred through the subsequent steps until the last integration step is reached. At the final step the result is the n-th order Taylor expansion of the flow of the initial value problem (2.1) at the final time t_f. Thus, the expansion of the flow of a dynamical system can be computed up to order n with fixed amount of effort.

The previous DA-based numerical integrators pave the way to numerous practical applications, some of them being addressed in the remaining of this

work. A first example is presented hereafter pertaining to the propagation of errors on initial conditions. The Taylor polynomials resulting from the use of DA-based numerical integrators expand the solution of the initial value problem (2.1) with respect to the initial condition. Thus, at each integration step, the dependence of the solution x_k on the value of the initial condition x_i is available in terms of a polynomial map $\mathcal{M}_{x_k}(\delta x_i)$, where δx_i is the displacement of the initial condition x_i from the reference value x_i^0. Suppose now the reference value x_i^0 represents a nominal initial condition for a dynamical system, and assume some error δx_i occurs between the actual initial condition x_i and the nominal one. The evaluation of the Taylor polynomial $\mathcal{M}_{x_k}(\delta x_i)$ readily supplies the new solution x_k at time t_k corresponding to the displaced initial condition. More precisely, the Taylor polynomial $\mathcal{M}_{x_k}(\delta x_i)$ delivers a Taylor approximation of the new solution x_k, whose accuracy depends on the expansion order n and the size of the displacement δx_i. The main advantage of the DA-based integrator is that the new solution is obtained by means of the evaluation of a polynomial, so avoiding a new numerical integration corresponding to the displaced initial condition. Moreover, the same Taylor polynomial can be used to identify the solution corresponding to any error δx_i. Consequently, if many values of δx_i are to be processed, multiple simple polynomial evaluations can be efficiently performed in place of multiple intensive numerical integrations.

The results of the application of the previous procedure are illustrated in the following example. The dynamics of an object moving in the Solar System is integrated in the framework of the two body problem:

$$\begin{cases} \dot{\boldsymbol{r}} &= \boldsymbol{v} \\ \dot{\boldsymbol{v}} &= -\frac{\mu}{r^3}\,\boldsymbol{r}, \end{cases} \tag{2.5}$$

where $\boldsymbol{r}$ and $\boldsymbol{v}$ are the object position and velocity respectively, and μ is the Sun gravitational parameter. The nominal initial conditions are set such that the object starts moving from the pericenter of an elliptic orbit, lying on the ecliptic plane (see the dotted line in Fig. 2.2a). The pericenter radius is 1 AU, whereas the magnitude of the initial velocity is selected to have a resulting orbit of eccentricity 0.5. A DA-based 8-th order Runge–Kutta–Fehlberg (RKF78) scheme is used to expand the solution of the ODE (2.5) along one revolution of the resulting orbit. A box of initial positions 0.01 AU on each side is considered and its evolution is investigated. Given the bijectivity of the flow of (2.5), the boundary points of the initial uncertainty box propagate into boundary points of the corresponding solution set at each integration time. Consequently, the evolution of the initial box is studied by evolving its boundary. Based on the previous observation, a uniform

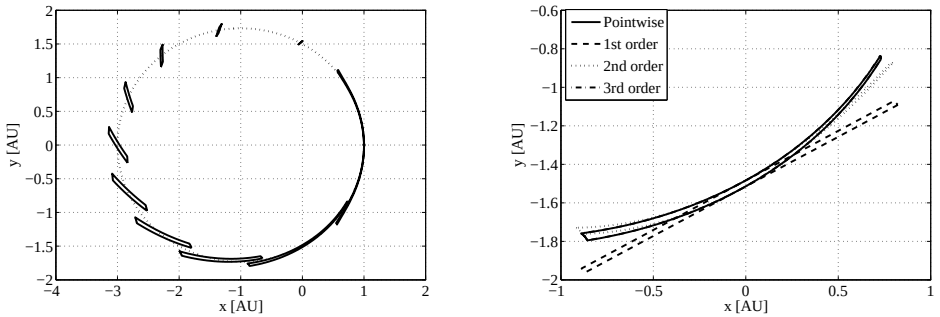

Figure 2.2: (**a**) Propagation of a box of initial positions in the two-body problem using the 5-th order expansion of the flow of the associated ODE; (**b**) accuracy analysis on one of the resulting boxes.

sampling of the boundary of the initial box is performed; for each sample, the displacement with respect to the nominal initial conditions is computed and the polynomial maps obtained by means of the DA-based integrator are evaluated. In this way, for each integration time, the evolved box can be readily plotted by means of mere polynomial evaluations. The evolved box is reported in Fig. 2.2a corresponding to 10 integration times uniformly distributed over the orbital period, using a 5-th order expansion of the flow of the ODE in (2.5). The time required by COSY-Infinity for the computation of the 5-th order map is about 0.38 s on a 2 GHz Intel Core Duo MacBook running Mac OS X.

The accuracy of the Taylor expansion of the flow is better highlighted in Fig. 2.2b. Focusing on a particular integration time, the exact propagated box is reported (solid line), which is based on a multiple point-wise integration of the samples. The propagated boxes obtained by the evaluation of the polynomial maps representing the flow of the ODE in (2.5) are then plotted for comparison, corresponding to different expansion orders. The figure shows that an accurate representation of the flow is already achieved using a 5-th order expansion.

Finally, it is worth mentioning that the same procedure can be used to compute the dependence of the solution with respect to either the initial integration time, t_i, or the final one, t_f. Without loss of generality, suppose the Taylor expansion of the solution of the initial value problem (2.1) with respect to the final time t_f is of interest (this is needed in the algorithm presented in Chapter 5). It is convenient in this case to perform a time transformation by setting $t = \tau\ (t_f - t_i)$, where τ is the new independent

variable. The dynamics in (2.1) is then extended to

$$\begin{cases} \dfrac{\mathrm{d}x}{\mathrm{d}\tau} &= (t_f - t_i) \cdot \ f(x, t(\tau)) \\ \dfrac{\mathrm{d}s}{\mathrm{d}\tau} &= 0, \end{cases} \tag{2.6}$$

with the initial condition $s(0) = s_i = (t_f - t_i)$ for the adjoint variable s. The integration of (2.1) in the time interval $t \in [t_i, t_f]$ is now reduced to the integration of (2.6) in the time interval $\tau \in [0, 1]$. The final time is now part of the initial conditions and appears as a parameter of the augmented dynamics. The initial condition x_i and the final time t_f can then be replaced by their DA representatives $[x_i] = x_i + \delta x_i$ and $[t_f] = t_f + \delta t_f$. Similarly to before, performing all the operations of the numerical integration in the framework of differential algebra allows to compute the Taylor expansion of the solution with respect to the initial condition and the final time at each step.

2.3 Notes on Taylor Models

As detailed in chapters 4 and 5, the computation of propellant margins using DA techniques relies on the necessity of bounding Taylor polynomials over admissible error sets. Several methods are available in the literature to achieve this goal. For example, the commonly used interval approach has excelled in solving this problem elegantly from both a formal and an implementational viewpoint. However, there are situations where the method has limitations for extended or complicated calculations because of the dependency problem, which is characterized by a cancellation of various sub-parts of the function that cannot be detected by direct use of interval methods. This effect often leads to pessimism and sometimes even drastic overestimation of range enclosure.

The Taylor model approach is proposed and used in this work. Taylor models enable the computation of fully mathematically rigorous range enclosures while largely avoiding many of the limitations of the conventional interval method. The method is based on the inductive local modelling of functional dependencies by a polynomial with a rigorous remainder bound, and as such represents a hybrid between differential algebra and interval methods [27].

An n-th order Taylor model of a multivariate function f that is $(n + 1)$ times continuously partially differentiable on the domain D, consists of the n-th order multivariate Taylor polynomial P expanded around a point $\boldsymbol{x}_0 \in$

D and representing a high-order approximation of the function f, and a remainder error bound interval I for verification such that

$$\forall \boldsymbol{x} \in D, \quad f(\boldsymbol{x}) \in P(\boldsymbol{x} - \boldsymbol{x}_0) + I. \tag{2.7}$$

From Taylor's theorem, it is clear that the width of the remainder interval I can be chosen to scale with the domain size proportional to $(\boldsymbol{x} - \boldsymbol{x}_0)^{n+1}$. The practical computation of P and I is based on Taylor model arithmetic, which carries P and I trough all the operations comprising I. By choosing the size $|\boldsymbol{x} - \boldsymbol{x}_0|$ small and the order n sufficiently high, the size of the remainder interval I can be kept very small in practice. The bulk of the functional dependency is kept in the polynomial part P with point coefficients, and there is no interval arithmetic associated inflation that happens in the polynomial part. Thus, the interval related overestimation is rather optimally suppressed with the Taylor model method [27].

Altogether, the Taylor model approach has the following important properties:

1. The ability to provide enclosures of any function given by a finite computer code list by a Taylor polynomial and a remainder bound with a sharpness that scales with order $(n + 1)$ of the width of the domain.

2. The computational expense increases only moderately with order, allowing the computation of sharp range enclosures even for complicated functional dependencies with significant dependency problem.

3. The computational expense of higher dimensions increases only very moderately, significantly reducing the "curse of dimensionality".

The method is fully implemented in the code COSY Infinity [11].

The structure of Taylor models naturally represents a rich resource of information. In particular, the coefficients of the polynomial part P of a Taylor model are nothing but the derivatives up to order n. That means when representing a function f by a Taylor model (P, I) on a computer, we also obtain the local slope, Hessian and higher order derivatives free. When a task is focused on range bounding, those pieces of information become particularly useful.

While naive range bounding of Taylor models, namely merely evaluating each monomial of P using interval arithmetic then summing up all the contributions as well as the remainder interval I, already exhibits the superiority over the mere interval arithmetic, the active utilization of those additional pieces of information in Taylor models has a lot of potential of developing efficient range bounders. Based on this observation, various kinds of Taylor

model based range bounders have been developed [10]. Among them, the linear dominated bounder (LDB) is used in this work. The linear dominated bounder (LDB) is based on the fact that, for Taylor models with sufficiently small remainder bound, the linear part of the Taylor model dominates the behavior, and this is also the case for range bounding. More details on polynomial bounders are given in [28].

Chapter 3

Fuel-Optimal Low-Thrust Transfer Problem

This chapter addresses the fuel-optimal low-thrust transfer problem between two reference boundary states. The theoretical framework is provided and a smoothing method is presented to obtain the corresponding optimal reference trajectory. The application to a transfer to asteroid 1996 FG_3 is illustrated.

3.1 Optimal Control Problem

The optimal transfer problem and the numerical approach adopted to compute its reference solution are now introduced. It is assumed that the spacecraft is subject to Sun's gravity and its own thrust T, only. Two control variables associated to spacecraft thrust are considered: the thrust ratio $u \in [0, 1]$ and its direction $\boldsymbol{\alpha}$. The equation of the dynamics for the spacecraft position $\boldsymbol{r}$, velocity $\boldsymbol{v}$, and mass m, are

$$\begin{cases} \dot{\boldsymbol{r}} = \boldsymbol{v} \\ \dot{\boldsymbol{v}} = -\dfrac{\mu}{r^3}\,\boldsymbol{r} + c_1 \dfrac{u}{m}\,\boldsymbol{\alpha} \\ \dot{m} = -c_2\,u. \end{cases} \tag{3.1}$$

The two constants c_1 and c_2 in Eq. (3.1) are defined as

$$\begin{aligned} c_1 &= T_{\max} \\ c_2 &= \frac{T_{\max}}{I_{\mathrm{sp}}\,g_0}, \end{aligned}$$

and μ is the gravitational constant of the Sun. The dynamics are normalized choosing the astronomical unit (AU), the initial mass of the spacecraft, and the velocity on a circular orbit of radius 1 AU as reference units.

The goal is to minimize the propellant necessary to transfer the spacecraft between two fixed states in a given time of flight. This is achieved by defining an optimal control problem in which the objective function to be minimized is

$$J = c_2 \int_{t_0}^{t_f} u \, dt, \tag{3.2}$$

subject to the set of nonlinear constraints

$$\begin{cases} \boldsymbol{r}(t_0) = \boldsymbol{r}_0 \\ \boldsymbol{v}(t_0) = \boldsymbol{v}_0 \\ m(t_0) = 1 \\ \boldsymbol{r}(t_f) = \boldsymbol{r}_f \\ \boldsymbol{v}(t_f) = \boldsymbol{v}_f. \end{cases} \tag{3.3}$$

In an interplanetary transfer, the constraints on the initial and final positions are associated to the initial and final positions of the departure and arrival bodies. Thus, once the initial epoch t_0 and the final epoch t_f (or the time of flight t_{ToF}, so that $t_f = t_0 + t_{ToF}$) are chosen, $\boldsymbol{r}_0$ and $\boldsymbol{r}_f$ are available via ephemeris evaluations. As a rendezvous problem is considered here, $\boldsymbol{v}_f$ coincides with the velocity of the arrival body, computed with the same ephemeris function. On the other hand, $\boldsymbol{v}_0$ can include the contribution given by the launcher, thus $\boldsymbol{v}_0 = \boldsymbol{v}_E(t_0) + \Delta\boldsymbol{v}$, in which $\boldsymbol{v}_E(t_0)$ is the velocity of the Earth at the departure epoch.

Through Pontryagin's maximum principle the optimal control problem is reduced to a two-point boundary value problem (TPBVP). First the costate vector $\boldsymbol{\lambda} = [\boldsymbol{\lambda}_r,\ \boldsymbol{\lambda}_v,\ \lambda_m]$ is introduced, together with the Hamiltonian

$$H = \boldsymbol{\lambda}_r \cdot \boldsymbol{v} + \boldsymbol{\lambda}_v \cdot \left(-\frac{\mu}{r^3}\boldsymbol{r} + c_1 \frac{u}{m}\boldsymbol{\alpha} \right) - \lambda_m c_2 u + c_2 u. \tag{3.4}$$

The optimal thrust direction and magnitude, which minimize the Hamiltonian in Eq. (3.4), are

$$\boldsymbol{\alpha} = -\frac{\boldsymbol{\lambda}_v}{\lambda_v} \tag{3.5}$$

$$\begin{cases} u = 0 & \text{if } \rho > 0 \\ u = 1 & \text{if } \rho < 0 \\ u \in [0,1] & \text{if } \rho = 0, \end{cases} \tag{3.6}$$

where the switching function ρ is

$$\rho = 1 - \frac{c_1 \lambda_v}{c_2 m} - \lambda_m. \tag{3.7}$$

The dynamics of the costate is given by

$$\begin{cases} \dot{\boldsymbol{\lambda}}_r = \dfrac{\mu}{r^3}\boldsymbol{\lambda}_v - \dfrac{3\,\mu\,\boldsymbol{r}\cdot\boldsymbol{\lambda}_v}{r^5}\,\boldsymbol{r} \\ \dot{\boldsymbol{\lambda}}_v = -\boldsymbol{\lambda}_r \\ \dot{\boldsymbol{\lambda}}_m = -c_1\,\dfrac{u}{m^2}\,\lambda_v. \end{cases} \tag{3.8}$$

According to the transversality condition, the only constraint for the costates is

$$\lambda_m(t_f) = 0, \tag{3.9}$$

since the final mass is free.

The optimal control problem is reduced to a TPBVP defined by the dynamics of the state and costate (3.1) and (3.8), the optimality conditions (3.5) and (3.6), and the constraints (3.3) and (3.9). This problem will be referred to as fuel-optimal problem (FOP) in the remainder of the paper. For details on the optimal control problem formulation the reader may refer to Reference [13].

3.1.1 Numerical solution of the optimal control problem

The numerical solution of the TPBVP is difficult because of the small convergence radius, the sensitivity of the initial guesses, the discontinuous integrated functions, and the singular Jacobian matrix. A common practice is to use an homotopic approach by perturbing the performance index with the introduction of a parameter in the range $[0, 1]$. The procedure starts with a unitary value of the parameter, for which the numerical solution is easily computed. The FOP is solved by continuously decreasing the perturbation parameter from one to zero and taking the obtained solution as an initial guess for the next iteration [24].

An alternative approach, based on a C^∞ approximation of the discontinuous optimal control law, is here proposed. The method is based on a three-step procedure and it exhibits high numerical robustness, as C^∞ TPBVP are solved in the first two steps. Furthermore, the second step delivers a solution that is so close to the one of the FOP that numerical convergence is guaranteed.

Step 1: energy-optimal problem

As a first step, an energy-optimal problem (EOP) is formulated. The constraint on the maximum thrust is removed and the objective function is redefined as

$$J = \frac{1}{2}\int_{t_0}^{t_f} a^2\, dt, \tag{3.10}$$

where $\boldsymbol{a}$ is the acceleration vector given by the thruster. The equations of motion for the spacecraft reduce to

$$\begin{cases} \dot{\boldsymbol{r}} = \boldsymbol{v} \\ \dot{\boldsymbol{v}} = -\dfrac{\mu}{r^3}\,\boldsymbol{r} + \boldsymbol{a} \\ \dot{m} = -\dfrac{c_2}{c_1}\,u\,m, \end{cases} \tag{3.11}$$

and the optimality condition to

$$\boldsymbol{a} = -\boldsymbol{\lambda}_v. \tag{3.12}$$

The mass multiplier is identically zero during the transfer, whereas the dynamics for the position and velocity multipliers read

$$\begin{cases} \dot{\boldsymbol{\lambda}}_r = \dfrac{\mu}{r^3}\boldsymbol{\lambda}_v - \dfrac{3\,\mu\,\boldsymbol{r}\cdot\boldsymbol{\lambda}_v}{r^5}\,\boldsymbol{r} \\ \dot{\boldsymbol{\lambda}}_v = -\boldsymbol{\lambda}_r. \end{cases} \tag{3.13}$$

The set of constraints on the position and the velocity (3.3) remains unchanged. The TPBVP for the EOP is continuous and its solution can be easily obtained by standard nonlinear equations solvers, starting from the initial guess $\boldsymbol{\lambda}_r = \boldsymbol{0}$ and $\boldsymbol{\lambda}_v = \boldsymbol{0}$. The solution of the TPBVP is embedded in a parametric optimization problem, in which t_0, t_{ToF}, and $\Delta\boldsymbol{v}$ are also optimized. (Note that this aspect can be included in the formulation of the optimal control problem, but this approach has been avoided to keep the TPBVP as simple as possible). A vector of optimization variables is defined as

$$\boldsymbol{x} = [t_0, t_{ToF}, \Delta\boldsymbol{v}, \boldsymbol{\lambda}_{r_0}, \boldsymbol{\lambda}_{v_0}], \tag{3.14}$$

and the search space is limited by upper and lower bounds (the initial Lagrangian multipliers are left unbounded). The objective function to be minimized is

$$J = -m_f \tag{3.15}$$

and the set of constrains are

$$\begin{cases} \boldsymbol{r}\left(t_f\right) = \boldsymbol{r}_f \\ \boldsymbol{v}\left(t_f\right) = \boldsymbol{v}_f \\ \Delta v \leq \Delta v_{\max} \end{cases} \tag{3.16}$$

where $\Delta v_{\max}$ is the maximum value for launcher's contribution. For given arrival body, starting from an initial guess $\boldsymbol{x}_0$ (where the initial value for the Lagrangian multipliers are set to zero), the optimization process:

1. Computes $\boldsymbol{r}_0$ and $\boldsymbol{v}_0 = \boldsymbol{v}_E(t_0)+\Delta\boldsymbol{v}$ at t_0, and $\boldsymbol{r}_f$ and $\boldsymbol{v}_f$ at $t_f = t0+t_{T0F}$ by ephemeris evaluation

2. Integrates the dynamics (3.11) and (3.13) from t_0 to t_f, with the optimal acceleration profile defined by $\boldsymbol{a} = -\boldsymbol{\lambda}_v$

3. Evaluates the objective function (3.15) and the constraints (3.16)

4. Iterates until the constraints are satisfied to a given accuracy and objective function is minimized

A nonlinear quadratic programming method is used for the optimization.

Step 2: continuous fuel-optimal problem

The optimal values found for $\boldsymbol{x}$ are used to initiate the second step of the numerical procedure. In this stage the values of t_0, t_{ToF}, and $\Delta\boldsymbol{v}$ are frozen, whereas those for the initial Lagrangian multipliers are used as initial guesses of a new optimal control problem. This problem is the same as the FOP, but the discontinuous law for the thrust ratio is approximated by a C^∞ function. In particular, an exponential representation is chosen

$$u = \frac{1}{1 + e^{p\,\rho}}, \tag{3.17}$$

where ρ is the switching function, and p a continuation parameter. For increasing values of p the continuous representation of u tends to the optimal bang-bang solution of the FOP. The availability of a first guess for the Lagrangian multipliers and the continuos representation of the optimal control law enable the solution of the TPBVP with standard nonlinear equation solvers. A starting value of one for the continuation parameter is usually considered. Then, this value is progressively increased until the expected bang-bang structure appears.

Step 3: discontinuos fuel-optimal problem

Finally, in last step of the procedure, the TPBVP associated to the FOP is solved with a fifth order finite difference method.

3.2 Reference trajectories

A rendezvous with asteroid 1996 FG_3 is considered. This asteroid is a near-Earth minor planet in the Apollo group and it is the primary target of the European Space Agency's Marco Polo-R mission. A spacecraft with initial mass of 1500 kg is selected. The propulsive system is characterized by thrusting capability of 0.33 N and specific impulse of 3800 s. In the following three reference solutions are presented; each of them is characterized by a different number of thrust arcs.

3.2.1 2-bang reference trajectory

The reference solution with two thrust arcs is presented. Departure date t_0 in the interval $[4900, 5500]$ MJD2000 is considered and the time of flight t_{ToF} is constrained to $[350, 550]$ days. The maximum value for the launcher Δv is 1 km/s .

For the EOP, the guesses for the t_0 and t_{ToF} are 5200 MJD2000 and 480 days, respectively. Null initial values for both the Δv and the Lagrangian multipliers are used. The optimal solution is characterized by $t_0 = 5314.645$ MJD2000, whereas the t_{ToF} and Δv hit their lower and upper bounds, respectively. The mass at rendezvous is 1304.86 kg. The thrust magnitude associated to this solution is plotted with the dotted line in Figure 3.1(c). Note that the maximum thrust exceeds the thrust available on board, but this is compatible with the EOP formulation.

The solution of the EOP is taken as first guess for the second step. Here both the t_0 and t_{ToF} are fixed, and a sequence of ten TPBVP is solved for increasing values of the continuation parameter p. These solutions are plotted with dashed lines in Figure 3.1(c), where the emergence of the bang-bang structure is clearly visible.

In the third step the FOP is addressed. With few iterations, the TPBVP solver computes the optimal discontinuous control law, which allows for a final spacecraft mass of 1313.68 kg. The thrust components of the discontinuous solution of the FOP problem are shown in Figure 3.1(d). The projection of the optimal interplanetary transfer in the $x - y$ plane is shown in Figure 3.1(a) and the associated switching function in Figure 3.1(b).

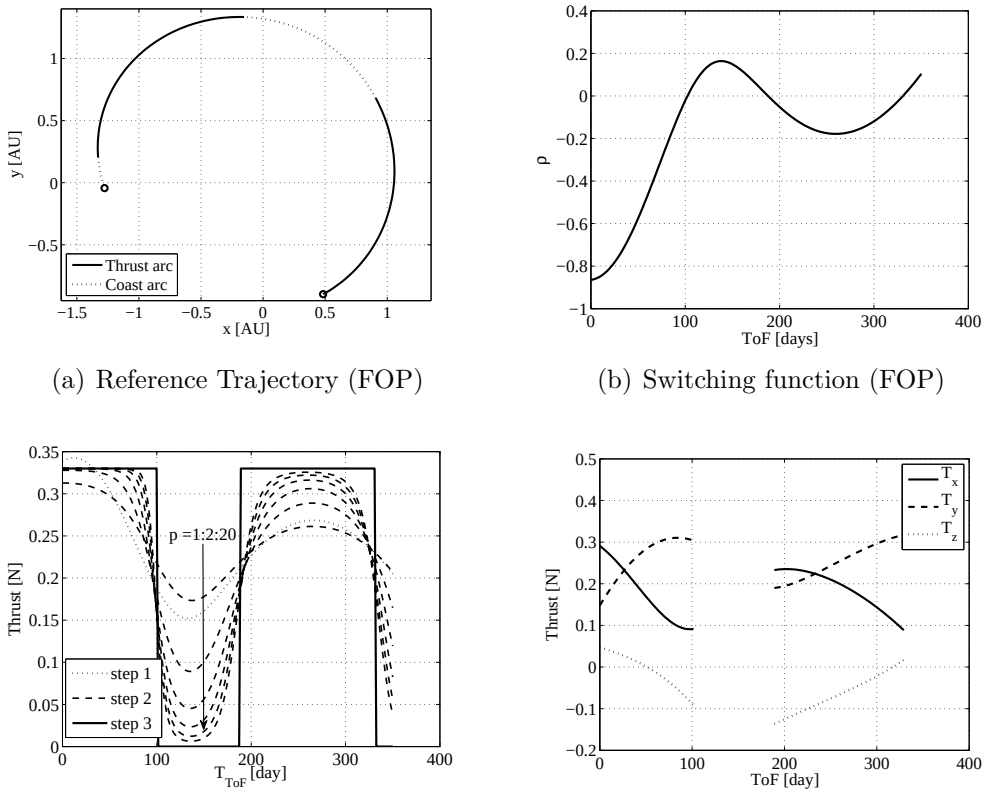

(a) Reference Trajectory (FOP)

(b) Switching function (FOP)

(c) Control magnitude (three-step procedure)

(d) Control components (FOP)

Figure 3.1: 2-bang Earth–1996 FG_3 optimal transfer

Table 3.1 summarizes the main features of the two-bang reference solution.

3.2.2 3-bang reference trajectory

The reference solution with three thrust arcs is presented. The launch window $[4900, 5500]$ MJD2000 is considered and the t_{ToF} is constrained to $[700, 1200]$ days. The maximum launcher Δv is 0.6 km/s. The same 3-step procedure described in Section 3.2.1 is adopted to find the solution of the discontinuous FOP. In Figure 3.2 the solution found is plotted and the main details of the transfer are summarized in Table 3.2. Note that the solution involves almost two revolutions and the thrust arcs are concentrated at perihelion and aphelion.

Table 3.1: 2-bang solution details.

Departure Epoch	mjd2000	5314.63
Time of Flight	days	350.26
Final mass	kg	1313.68
Launcher Δv		
Δv_x	m/s	794.24
Δv_y	m/s	501.67
Δv_z	m/s	155.72
Switching times		
t_1	day	100.59
t_2	day	188.09
t_3	day	331.03

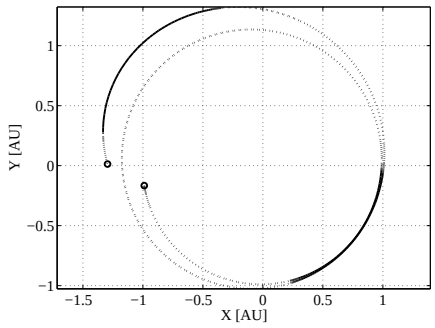

(a) Reference Tarjectory (FOP)

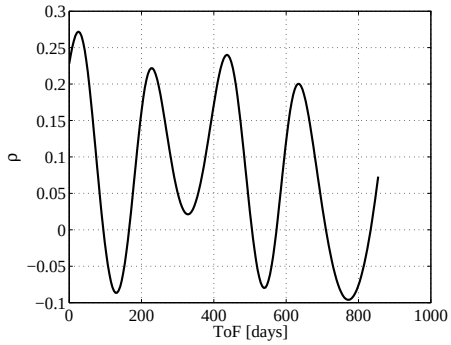

(b) Switching function (FOP)

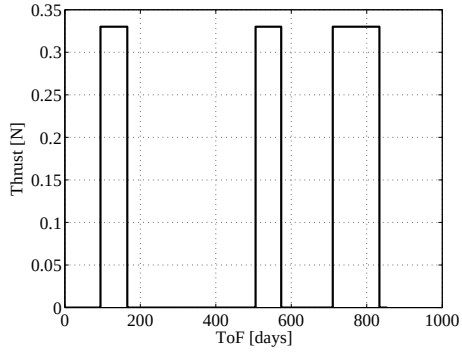

(c) Control magnitude (FOP)

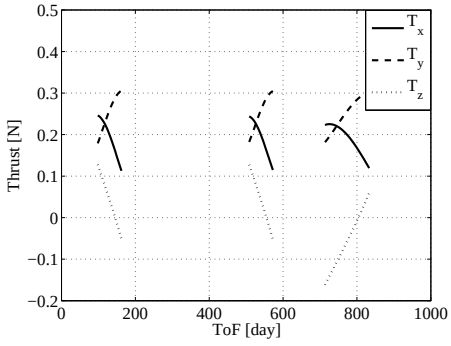

(d) Control components (FOP)

Figure 3.2: 3-bang Earth–1996 FG_3 optimal transfer

Table 3.2: 3-bang solution details.

Departure Epoch	mjd2000	5201.82
Time of Flight	days	850.43
Final mass	kg	1299.12
Launcher Δv		
Δv_x	m/s	435.84
Δv_y	m/s	308.87
Δv_z	m/s	27.12
Switching times		
t_1	day	94.45
t_2	day	165.58
t_3	day	505.42
t_4	day	573.29
t_5	day	709.98
t_6	day	833.55

3.2.3 4-bang reference trajectory

The reference solution with four thrust arcs is presented. The launch window is the same of the previous transfers, whereas the t_{ToF} is constrained to $[700, 800]$ days. The launcher Δv is reduce to 0.2 km/s in order to increase the number of thrust arcs. The same 3-step procedure described in Section 3.2.1 is adopted for the solution of the FOP. In Figure 3.3 the solution is plotted and the main details of the transfer are summarized in Table 3.3.

Table 3.3: 4-bang solution details.

Departure Epoch	mjd2000	5203.20
Time of Flight	days	800.00
Final mass	kg	1282.17
Launch Δv		
Δv_x	m/s	-13.86
Δv_y	m/s	-198.73
Δv_z	m/s	17.71
Switching times		
t_1	day	96.45
t_2	day	185.89
t_3	day	326.05
t_4	day	388.04
t_5	day	535.97
t_6	day	585.17
t_7	day	715.92

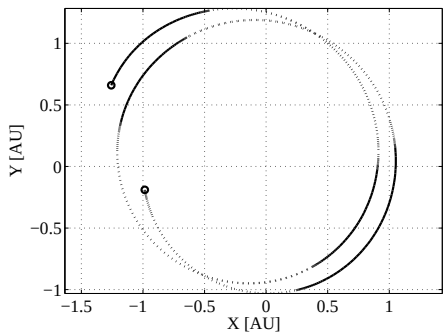

(a) Reference Trajectory (FOP)

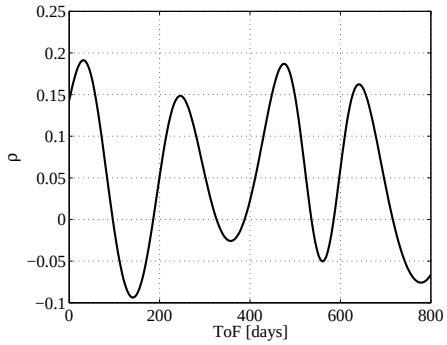

(b) Switching function (FOP)

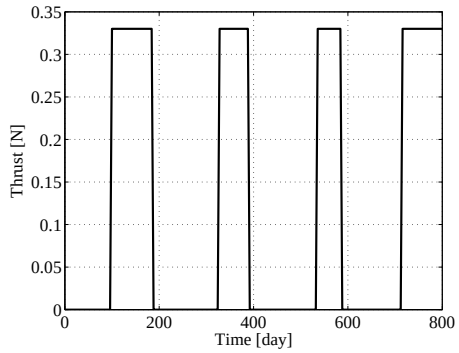

(c) Control magnitude (FOP)

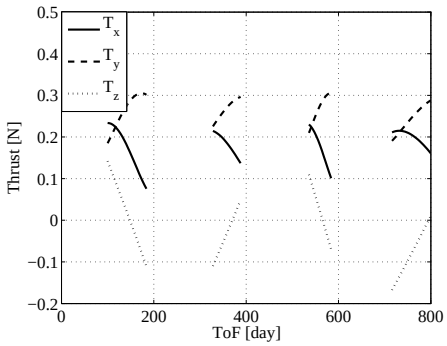

(d) Control components (FOP)

Figure 3.3: 4-bang Earth–1996 FG_3 optimal transfer

Chapter 4

High order expansion of the fuel-optimal smooth solution

With reference to the three-step procedure for the solution of the fuel-optimal control problem reported in Section 3.1.1, the algorithm for the high order expansion of the continuous solution at the end of the second step is introduced in this chapter. As shown in Chapter 4, the second step delivers a solution that is very close to the exact bang-bang solution of the FOP. At the same time, it guarantees analyticity by using a $\mathcal{C}^\infty$ approximation of the control. The lack of control switches eases the computation of its high order expansion with respect to boundary conditions, while the continuation process assures adequate accuracy of the result. The performances of the algorithm are assessed on the transfer to asteroid 1996 FG_3, considering different reference solutions. The accuracy of the expansions are provided and its limits discussed.

4.1 DA algorithm for the fuel-optimal smooth solution

Assume a reference solution of the FOP (3.1)-(3.3) is available. Thus, the initial costates, $\boldsymbol{\lambda}_{x_0} = [\boldsymbol{\lambda}_{r_0}, \boldsymbol{\lambda}_{v_0}]$ and λ_{m_0}, the final costates, $\boldsymbol{\lambda}_{x_f} = \left[\boldsymbol{\lambda}_{r_f}, \boldsymbol{\lambda}_{v_f}\right]$ and λ_{m_f}, have been computed for assigned initial conditions, $\boldsymbol{x_0} = [\boldsymbol{r}_0, \boldsymbol{v}_0]$ and m_0, and final target position and velocity $\boldsymbol{x_f} = [\boldsymbol{r}_f, \boldsymbol{v}_f]$. It is worth recalling that $\lambda_{m_f} = 0$ for the transversality condition. The DA algorithm for the arbitrary order expansion of the smooth approximation of the solution of the FOP with respect to both the initial spacecraft state and the final target state is based on the following steps.

Step 1. Initialize the initial spacecraft state and the initial costates as DA variables. This means the variations with respect to their reference values are considered:

$$\begin{aligned} [\boldsymbol{x}(t_0)] &= \boldsymbol{x}_0 + \delta\boldsymbol{x}_0 \\ [\boldsymbol{\lambda}_x(t_0)] &= \boldsymbol{\lambda}_{x0} + \delta\boldsymbol{\lambda}_{x0} \\ [\lambda_m(t_0)] &= \lambda_m + \delta\lambda_{m0}. \end{aligned} \tag{4.1}$$

Step 2. Using the techniques introduced in Section 2.2, perform a DA-based integration of the ODEs (3.1) and (3.8) from t_0 to t_f to obtain the high order expansion of the flow at t_f. More specifically, the dependence of the spacecraft state, mass, and costates on the perturbed initial conditions is obtained in terms of the high order polynomial map

$$\begin{pmatrix} [\boldsymbol{x}_f] \\ [m_f] \\ [\boldsymbol{\lambda}_{x_f}] \\ [\lambda_{m_f}] \end{pmatrix} = \begin{pmatrix} \boldsymbol{x}_f \\ m_f \\ \boldsymbol{\lambda}_{x_f} \\ \lambda_{m_f} \end{pmatrix} + \begin{pmatrix} \mathcal{M}_{\boldsymbol{x}_f} \\ \mathcal{M}_{m_f} \\ \mathcal{M}_{\boldsymbol{\lambda}_{x_f}} \\ \mathcal{M}_{\lambda_{m_f}} \end{pmatrix} \begin{pmatrix} \delta\boldsymbol{x}_0 \\ \delta\boldsymbol{\lambda}_{x_0} \\ \delta\lambda_{m_0} \end{pmatrix}, \tag{4.2}$$

where $\mathcal{M}_{\boldsymbol{x}_f}$, $\mathcal{M}_{m_f}$, $\mathcal{M}_{\boldsymbol{\lambda}_{x_f}}$, and $\mathcal{M}_{\lambda_{m_f}}$ denote high order polynomials in $\delta\boldsymbol{x}_0$, $\delta\boldsymbol{\lambda}_{x_0}$, and $\delta\lambda_{m_0}$.

Step 3. Compute $\delta\boldsymbol{x}_f = [\boldsymbol{x}_f] - \boldsymbol{x}_f$ and $\delta\lambda_{m_f} = \left[\lambda_{m_f}\right] - \lambda_{m_f}$, and consider the map

$$\begin{pmatrix} \delta\boldsymbol{x}_f \\ \delta\lambda_{m_f} \\ \delta\boldsymbol{x}_0 \end{pmatrix} = \begin{pmatrix} \mathcal{M}_{\boldsymbol{x}_f} \\ \mathcal{M}_{\lambda_{m_f}} \\ \mathcal{I}_{\delta\boldsymbol{x}_0} \end{pmatrix} \begin{pmatrix} \delta\boldsymbol{x}_0 \\ \delta\boldsymbol{\lambda}_{x_0} \\ \delta\lambda_{m_0} \end{pmatrix}, \tag{4.3}$$

which is built extracting the first and last components of map (4.2) and concatenating them with the identity maps for $\delta\boldsymbol{x}_0$.

Step 4. Invert the above map to obtain

$$\begin{pmatrix} \delta\boldsymbol{x}_0 \\ \delta\boldsymbol{\lambda}_{x_0} \\ \delta\lambda_{m_0} \end{pmatrix} = \begin{pmatrix} \mathcal{M}_{\boldsymbol{x}_f} \\ \mathcal{M}_{\lambda_{m_f}} \\ \mathcal{I}_{\delta\boldsymbol{x}_0} \end{pmatrix}^{-1} \begin{pmatrix} \delta\boldsymbol{x}_f \\ \delta\lambda_{m_f} \\ \delta\boldsymbol{x}_0 \end{pmatrix}. \tag{4.4}$$

Obtaining map (4.4) from map (4.3) involves inverting high order polynomials. This inversion can be easily performed in the DA framework by reducing the inversion problem to an equivalent fixed-point problem as described in [6]. The resulting map relates the initial state and costate to perturbations on the boundary states $\delta\boldsymbol{x}_0$ and $\delta\boldsymbol{x}_f$, and on the final mass costate.

Step 5. Impose the transversality condition on the mass costate by setting $\delta\lambda_{m_f} = 0$ in map (4.4). This yields

$$\begin{pmatrix} \delta \boldsymbol{x}_0 \\ \delta \boldsymbol{\lambda}_{x_0} \\ \delta\lambda_{m_0} \end{pmatrix} = \begin{pmatrix} \mathcal{M}_{\boldsymbol{x}_f} \\ \mathcal{M}_{\lambda_{m_f}} \\ \mathcal{I}_{\delta \boldsymbol{x}_0} \end{pmatrix}^{-1} \begin{pmatrix} \delta \boldsymbol{x}_f \\ 0 \\ \delta \boldsymbol{x}_0 \end{pmatrix}. \tag{4.5}$$

Step 6. Add the reference initial costate to the last two components of (4.5) to obtain the map

$$\begin{pmatrix} [\boldsymbol{\lambda}_{x_0}] \\ [\lambda_{m_0}] \end{pmatrix}_{\lambda_{m_f}=0} = \begin{pmatrix} \boldsymbol{\lambda}_{x_0} \\ \lambda_{m_0} \end{pmatrix} + \begin{pmatrix} \mathcal{M}_{\boldsymbol{\lambda}_{x_0}} \\ \mathcal{M}_{\lambda_{m_0}} \end{pmatrix}_{\lambda_{m_f}=0} \begin{pmatrix} \delta \boldsymbol{x}_0 \\ \delta \boldsymbol{x}_f \end{pmatrix} \tag{4.6}$$

Map (4.6) is the high order Taylor expansion of the solution of the optimal control problem with respect to the initial spacecraft state and the final target state. More specifically, for any perturbed $\delta \boldsymbol{x}_0$ and $\delta \boldsymbol{x}_f$, the evaluation of the polynomial map (4.6) delivers the associated optimal costates. It is worth observing that the polynomial map (4.6) supplies high order Taylor approximations of the solution of the optimal control problem for perturbed initial and final conditions, which are accurate up to the order used for the DA-based computation.

4.2 Transfer to 1996 FG_3: 2-bang solution

The performances of the algorithm introduced in the previous section are assessed on the Earth-1996 FG_3 transfer. The 2-bang reference trajectory reported in Section 3.2.1 is analyzed in this section. The fuel optimal transfer trajectory and control profile reported in Figures 3.1(a) and 3.1(c) are used as reference solution for the Taylor expansions. More specifically, the $\mathcal{C}^\infty$ approximation of the control profile at the end of the second step of the procedure in Section 3.1.1 is used and the algorithm is applied to compute a fourth order Taylor expansion of the solution of the FOP about the reference trajectory. Thus, the resulting map (4.6) is a fourth order polynomials in $\delta \boldsymbol{x}_0$ and $\delta \boldsymbol{x}_f$. The case of perturbed final target position is first investigated. The analysis for perturbed initial spacecraft position follows.

4.2.1 Perturbed final target position

The final position of asteroid 1996 FG_3, $\boldsymbol{r}_f$, is supposed to be affected by measurable errors. Given any displacement $\delta \boldsymbol{r}_f$ of the final target position

from its reference value, the polynomial map (4.6) is evaluated by setting $\delta\boldsymbol{x}_0 \equiv [\delta\boldsymbol{r}_0, \delta\boldsymbol{v}_0] = [0, 0]$ and $\delta\boldsymbol{x}_f \equiv [\delta\boldsymbol{r}_f, \delta\boldsymbol{v}_f] = [\delta\boldsymbol{r}_f, 0]$. The corresponding optimal values of $\boldsymbol{\lambda}_{x_0}$ and λ_{m_0} are computed. Then, starting from the reference initial spacecraft state and the new initial costates, a forward point-wise integration of the ODEs (3.1) and (3.8) supplies the optimal control law to transfer the spacecraft from the reference initial state to the perturbed final target position $\boldsymbol{r}_f + \delta\boldsymbol{r}_f$. A sketch of the performed simulation is reported in Figure 4.1, which illustrates also the error $\delta\tilde{\boldsymbol{r}}_f$ between the desired final position $\boldsymbol{r}_f + \delta\boldsymbol{r}_f$ and the actual final position reached by integrating the ODEs with the new costates, $\tilde{\boldsymbol{r}}_f$.

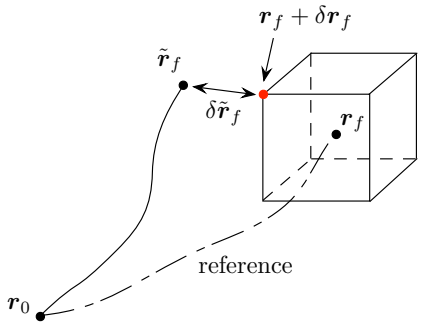

Figure 4.1: Illustration of the transfer to a perturbed final target position.

The performances of the procedure are studied hereafter. A maximum position error of 1E-3 AU is supposed to affect each component of the final target state. For each corner of the corresponding cube, the associated $\delta\boldsymbol{r}_f$ is computed and the map (4.6) is evaluated to obtain the new optimal transfer trajectory. For each sample, the maximum norm of the difference between the resulting trajectory $\tilde{\boldsymbol{r}}(t)$ and the reference trajectory $\boldsymbol{r}(t)$ is reported in Figure 4.2(a). Starting from the reference initial position, the new trajectories tend to move away from the reference along the transfer and reach the final imposed value of 1E-3 AU. A detail of all trajectories at arrival is reported in Figure 4.2(b). Thanks to the high order feedback, each new optimal trajectory hits the corresponding perturbed target.

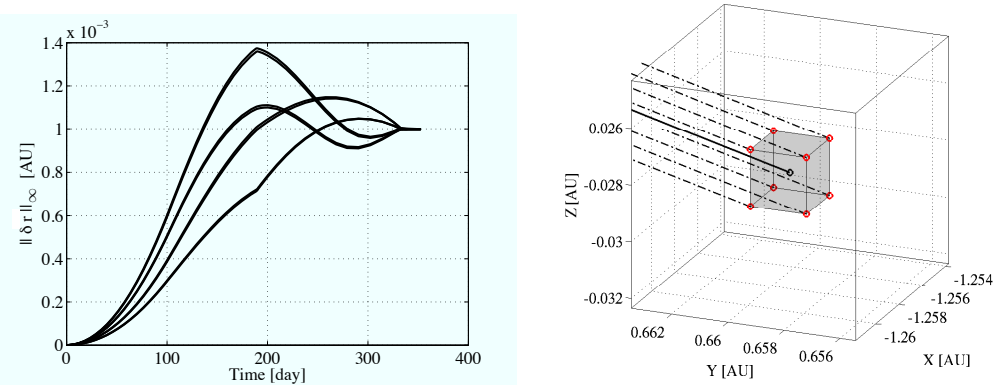

(a) Trajectory displacement along the transfer (b) Detail at arrival

Figure 4.2: 2-bang Earth–1996 FG_3 transfer: optimal feedback on perturbed final target positions.

Figure 4.3(a) plots the resulting optimal control magnitude profiles, whereas a detail on the second steep control variation is reported in Figure 4.3(b). The time at which thrust starts increasing changes with a maximum variation of approximately one day. For the sake of completeness, the feedback on the thrust direction is investigated in Figure 4.4(a). For each sample, the profiles of the components of the thrust vector are illustrated. A detail of the bang is reported in Figure 4.4(b).

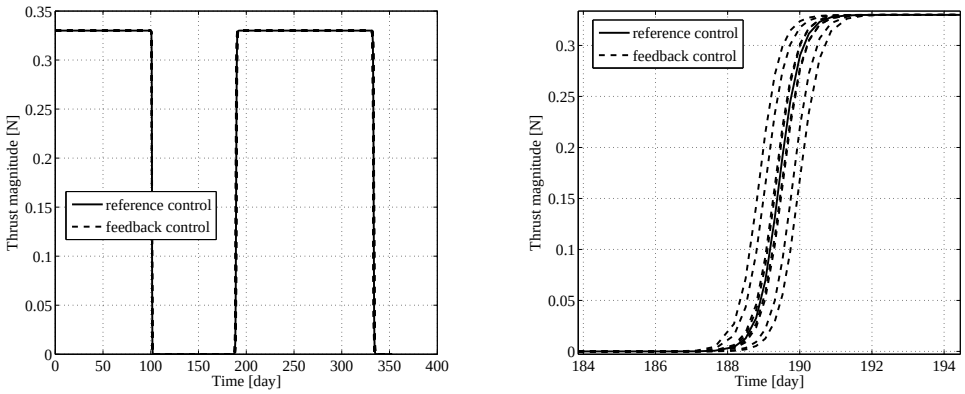

(a) Control profiles (b) Detail on second control switch

Figure 4.3: 2-bang Earth–1996 FG_3 transfer: optimal control profiles for perturbed final target positions.

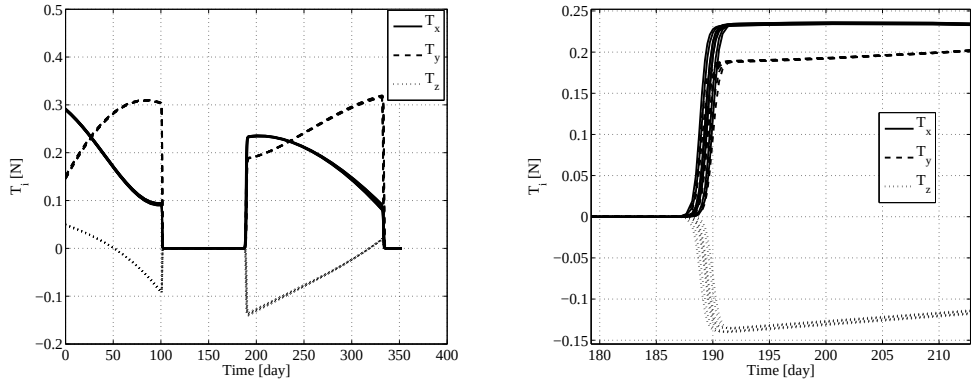

(a) Thrust components (b) Detail on second bang

Figure 4.4: 2-bang Earth–1996 FG_3 transfer: thrust components profiles for perturbed final target positions.

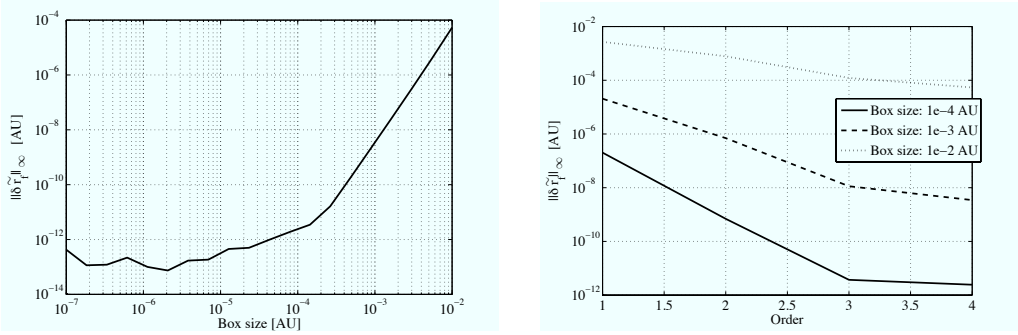

(a) Error vs. Box amplitude (b) Error vs. Order

Figure 4.5: 2-bang Earth–1996 FG_3 transfer: accuracy analysis for perturbed final target positions.

The accuracy of the fourth order map (4.6) is investigated in Figure 4.5(a). More specifically, the difference $\delta\tilde{\boldsymbol{r}}_f$ between the final position and the desired perturbed final target position is computed (refer to Figure 4.1 for an illustration of the defined quantities). The maximum norm for all samples is then reported. The same process is repeated for different box amplitudes. As expected, the error increases with box amplitude and the fourth order maps are adequate to compute control corrections for error boxes of amplitude up to 1E-2 AU, which is well above the errors to be managed in practical applications.

The effects of the order on the accuracy of the Taylor expansions is studied in Figure 4.5(b). The trend of $\delta\tilde{\boldsymbol{r}}_f$ is reported in figure for increasing

expansion orders and different error box amplitudes. The accuracy of the maps increases with order for all amplitudes analyzed. However, it is worth observing that, for an amplitude of 1E-2 AU, adequate values of $\delta\tilde{\boldsymbol{r}}_f$ are achieved only with expansions of order 3 or higher.

One of the main advantages of the DA-based algorithm of Section 4.1 lies in the availability of the functional dependency between the final spacecraft state and the perturbations, which can be profitably used to compute the propellant margins to compensate for the associated errors. More in detail, map (4.2) can be composed with map (4.5) to obtain

$$\begin{pmatrix} [\boldsymbol{x}_f] \\ [m_f] \\ [\boldsymbol{\lambda}_{x_f}] \\ [\lambda_{m_f}] \end{pmatrix}_{\lambda_{m_f}=0} = \begin{pmatrix} \boldsymbol{x}_f \\ m_f \\ \boldsymbol{\lambda}_{x_f} \\ \lambda_{m_f} \end{pmatrix} + \begin{pmatrix} \mathcal{M}_{\boldsymbol{x}_f} \\ \mathcal{M}_{m_f} \\ \mathcal{M}_{\boldsymbol{\lambda}_{x_f}} \\ \mathcal{M}_{\lambda_{m_f}} \end{pmatrix}_{\lambda_{m_f}=0} \begin{pmatrix} \delta\boldsymbol{x}_0 \\ \delta\boldsymbol{x}_f \end{pmatrix}. \tag{4.7}$$

The second component of map (4.7) can now be extracted:

$$[m_f]_{\lambda_{m_f}=0} = m_f + (\mathcal{M}_{m_f})_{\lambda_{m_f}=0}(\delta\boldsymbol{x}_0, \delta\boldsymbol{x}_f). \tag{4.8}$$

The polynomial (4.8) is the Taylor expansion of the optimal final spacecraft mass, i.e., for any perturbed initial and final state, the evaluation of map (4.8) gives the final spacecraft mass when the optimal control law (4.6) is applied to the spacecraft. The resulting map for the 2-bang Earth–1996 FG_3 transfer with perturbed final position is reported in Table 4.1.

In combination with the polynomial bounders, map (4.8) can be used to compute propellant margins. First of all, let us compute the Taylor expansion of the propellant mass with respect to the perturbed initial and final states. This can be achieved by subtracting (4.8) to the initial spacecraft wet mass m_0 for

$$[m_p]_{\lambda_{m_f}=0} = m_0 - [m_f]_{\lambda_{m_f}=0} = m_p + (\mathcal{M}_{m_p})_{\lambda_{m_f}=0}(\delta\boldsymbol{x}_0, \delta\boldsymbol{x}_f), \tag{4.9}$$

where m_p is the propellant mass consumed along the reference trajectory. Given any admissible interval set for $\delta\boldsymbol{x}_0$ and $\delta\boldsymbol{x}_f$, the polynomial bounder LDB introduced in Section 2.3 can be used to bound (4.9) and compute its range over the entire uncertainty set. Table 4.2 reports the resulting ranges for the 2-bang Earth–1996 FG_3 transfer under analysis, considering different error box amplitudes for the final target state. As expected, the reference propellent mass is inside the computed ranges. The propellent margins can be readily computed from the maximum and reference propellant masses. The results are reported in the same table.

Table 4.1: Polynomial map of the final mass for the perturbed final spacecraft position test case.

Coefficient	Order	Exponents		
		$\delta r^*_{f,x}$	$\delta r^*_{f,y}$	$\delta r^*_{f,z}$
0.8757870663524067	0	0	0	0
-0.2900633044823370E-04	1	1	0	0
-0.2260364816778009E-04	1	0	1	0
0.1678216656491956E-04	1	0	0	1
-0.9865666629785225E-07	2	2	0	0
0.5599331921764363E-07	2	1	1	0
-0.1135697287946365E-07	2	0	2	0
-0.2217197020532794E-08	2	1	0	1
-0.8818680973540418E-08	2	0	1	1
-0.2082481870432325E-07	2	0	0	2
0.9927284119231924E-10	3	3	0	0
-0.8465069238956000E-10	3	2	1	0
0.2960953157301605E-10	3	1	2	0
-0.3857043721815408E-11	3	0	3	0
-0.2255179223692822E-10	3	2	0	1
-0.7401363062267387E-12	3	1	1	1
0.6703761858078779E-11	3	0	2	1
0.2382333366347061E-11	3	1	0	2
0.3600443206631178E-11	3	0	1	2
-0.1582875682157064E-10	3	0	0	3
0.6310331618309671E-13	4	4	0	0
-0.5559264136148677E-13	4	3	1	0
0.3779870737207543E-13	4	2	2	0
-0.1171348301558188E-13	4	1	3	0
0.9134959419363138E-15	4	0	4	0
0.4228106979516125E-13	4	3	0	1
0.2150573156057715E-13	4	2	1	1
-0.3761301328578700E-14	4	1	2	1
-0.1847715518192562E-14	4	0	3	1
0.2942409627736531E-13	4	2	0	2
-0.7320076104625793E-15	4	1	1	2
0.8822995357803418E-15	4	0	2	2
0.2525082960379789E-14	4	1	0	3
0.2518381739858005E-13	4	0	1	3
-0.2146233917946829E-14	4	0	0	4

Table 4.2: 2-bang Earth–1996 FG_3 transfer: propellant margins for the perturbed final spacecraft position test case.

Reference m_p: 186.319 kg		
Box amplitude [AU]	m_p range [kg]	Margin [%]
1E-5	[186.309, 186.330]	0.006
1E-4	[186.217, 186.422]	0.055
1E-3	[185.303, 187.355]	0.556

4.2.2 Perturbed initial spacecraft position

Similarly to the previous section, the case of perturbed initial spacecraft position is now analyzed. The vector $\boldsymbol{r}_0$ is supposed to be affected by measurable errors. Given any $\delta\boldsymbol{r}_0$, the polynomial map (4.6) is evaluated at $\delta\boldsymbol{x}_0 = [\delta\boldsymbol{r}_0, 0]$ and $\delta\boldsymbol{x}_f = [0, 0]$. That is, for any initial position error, the optimal values of $\boldsymbol{\lambda}_{x_0}$ and λ_{m_0} to reach the reference position of 1996 FG_3 at t_f from the perturbed initial position are computed.

As in the case of perturbed final position, a maximum error of 1E-3 AU is supposed to affect each component of the initial spacecraft position. The corners of the associated cube are sampled and the map (4.6) is evaluated for the optimal correction of the initial costates and control profiles, as sketched in Figure 4.6.

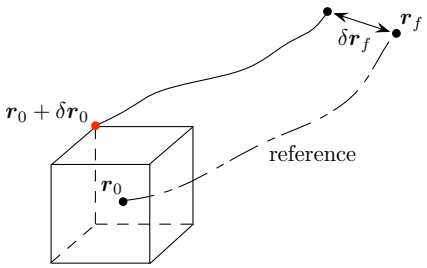

Figure 4.6: Illustration of the transfer from a perturbed initial spacecraft position.

For each sample, the maximum norm of the difference vector between the resulting trajectories $\tilde{\boldsymbol{r}}(t)$ and the reference trajectory $\boldsymbol{r}(t)$ is reported in Figure 4.7. Starting from the initial error 1E-3 AU, the new trajectories approach the reference along the transfer and cancel the error at t_f.

Figure 4.8(a) plots the resulting optimal control magnitude profiles, whereas Figure 4.8(b) reports a detail on the resulting first steep decrease of the con-

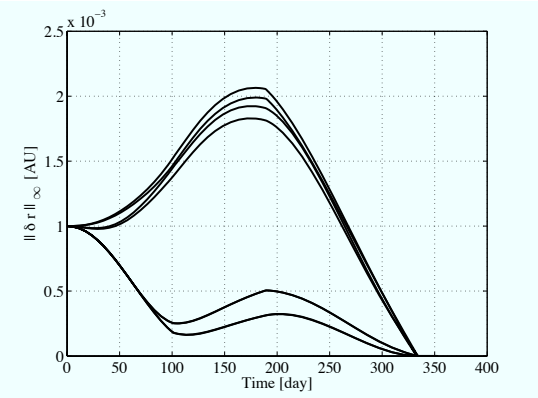

Figure 4.7: 2-bang Earth–1996 FG_3 transfer: optimal feedback on perturbed initial spacecraft positions. Trajectory displacement along the transfer.

trol action. The effect of the perturbed initial spacecraft positions on the control profiles is greater than in the case of perturbed final target positions, and the control switch varies within a range of about 5 days.

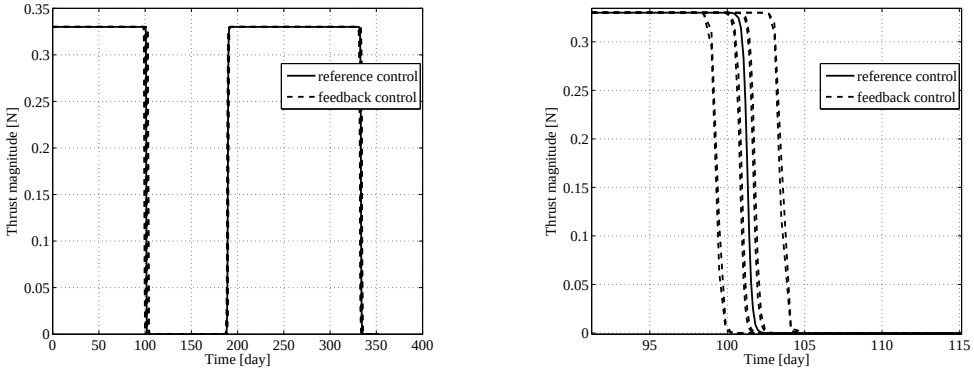

(a) Control profiles (b) Detail on first control switch

Figure 4.8: 2-bang Earth–1996 FG_3 transfer: optimal control profiles for perturbed initial spacecraft positions.

The thrust components profiles corresponding to each sample are reported in Figure 4.9(a), whereas a detail of the first bang is reported in Figure 4.9(b).

The accuracy of the fourth order maps (4.6) is investigated by computing the final position error $\delta \boldsymbol{r}_f$ with respect to the target (refer to Figure 4.6 for an illustration of the defined quantities). The maximum norm over all the samples is reported in Figure 4.10(a) for different box amplitudes. The error increases with box amplitude. A comparison between Figure 4.10(a) and

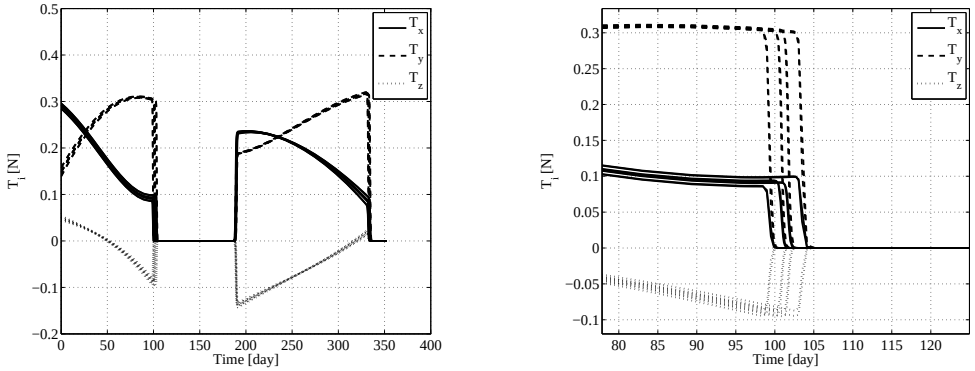

(a) Thrust components (b) Detail on first bang

Figure 4.9: 2-bang Earth–1996 FG_3 transfer: thrust components profiles for perturbed initial spacecraft positions.

Figure 4.5(a) shows that the map (4.6) are less accurate when used for the optimal feedback on the initial position. In this case the maps are sufficiently accurate to compute control corrections for error boxes of amplitude up to 1E-3 AU. As can be seen in Figure 4.10(b), the final position error for all expansion orders is too large for a box amplitude of 1E-2 AU.

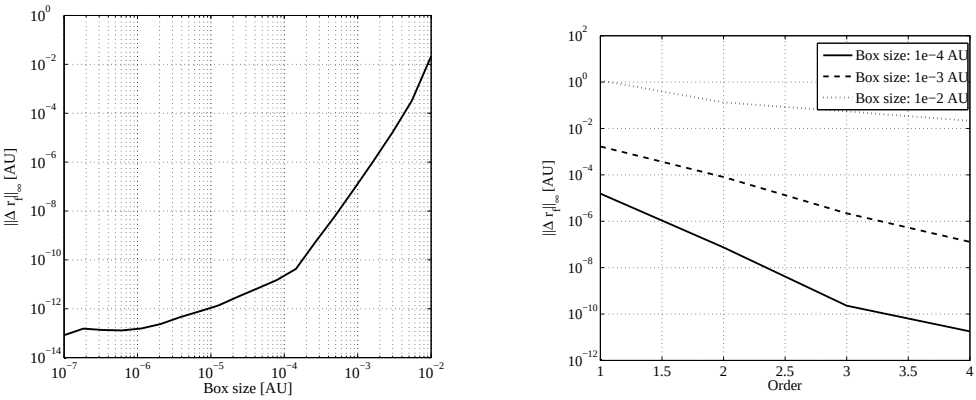

(a) Error vs. Box amplitude (b) Error vs. Order

Figure 4.10: 2-bang Earth–1996 FG_3 transfer: accuracy analysis for perturbed initial spacecraft positions.

Finally, similarly to the previous test case, the polynomial maps (4.8) and (4.9) are bounded for different error box amplitudes on the initial spacecraft position to compute propellant margins. The results are listed in Table 4.3.

Table 4.3: 2-bang Earth–1996 FG_3 transfer: propellant margins for the perturbed initial spacecraft position test case.

Reference m_p: 186.319 kg		
Box amplitude [AU]	m_p range [kg]	Margin [%]
1E-5	[186.298, 186.341]	0.012
1E-4	[186.107, 186.536]	0.116
1E-3	[184.348, 188.663]	1.258

4.3 Transfer to 1996 FG_3: 3-bang solution

The 3-bang reference trajectory to asteroid 1996 FG_3 (see Section 3.2.2) is now used as testbed for the algorithm. The fuel optimal transfer trajectory and control profile reported in Figures 3.2(a) and 3.2(c) are used as reference solution for the Taylor expansions. A fourth order map (4.6) is computed using the algorithm introduced in Section 4.1. Similarly to the 2-bang solution, the cases of perturbed final and initial position are investigated.

4.3.1 Perturbed final target position

The final position of asteroid 1996 FG_3, $\boldsymbol{r}_f$, is supposed to be affected by measurable errors and the polynomial map (4.6) is evaluated by setting $\delta\boldsymbol{x}_0 \equiv [\delta\boldsymbol{r}_0, \delta\boldsymbol{v}_0] = [0, 0]$ and $\delta\boldsymbol{x}_f \equiv [\delta\boldsymbol{r}_f, \delta\boldsymbol{v}_f] = [\delta\boldsymbol{r}_f, 0]$ to obtain the optimal corrections to compensate the errors. The new values of the initial costates are computed and forward point-wise integrations of the ODEs (3.1) and (3.8) are performed to transfer the spacecraft from the reference initial state to the perturbed final target position.

First of all, a maximum perturbation of 1E-3 AU is supposed to affect each component of the final target position. For each corner of the corresponding cube, the associated error with respect to the reference final state is computed and the map (4.6) is evaluated to obtain the new optimal transfer trajectory. Figure 4.11(a) plots the maximum norm of the difference between the resulting trajectory and the reference trajectory. The optimal feedback laws obtained with the fourth order corrections are able to guide the spacecraft from the reference initial state to the final imposed offset of 1E-3 AU. A detail of all trajectories at arrival is reported in Figure 4.11(b).

Figure 4.12(a) plots the resulting optimal control magnitude profiles and Figure 4.12(b) reports a detail on the second propelled arc. Similarly to the 2-bang test case, the optimal switching time for the sampled trajectories varies within a range of about 2 days. For the sake of completeness, the

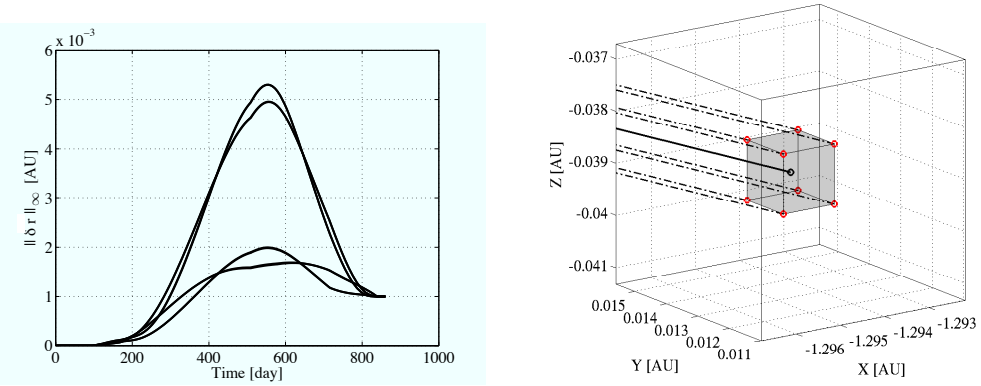

(a) Displacement along the transfer (b) Detail at arrival

Figure 4.11: 3-bang Earth–1996 FG_3 transfer: optimal feedback on perturbed final target positions.

feedback on the thrust direction is investigated in Figure 4.13(a). For each sample, the profiles of the components of the thrust vector are illustrated and a detail of the first bang is reported in Figure 4.13(b).

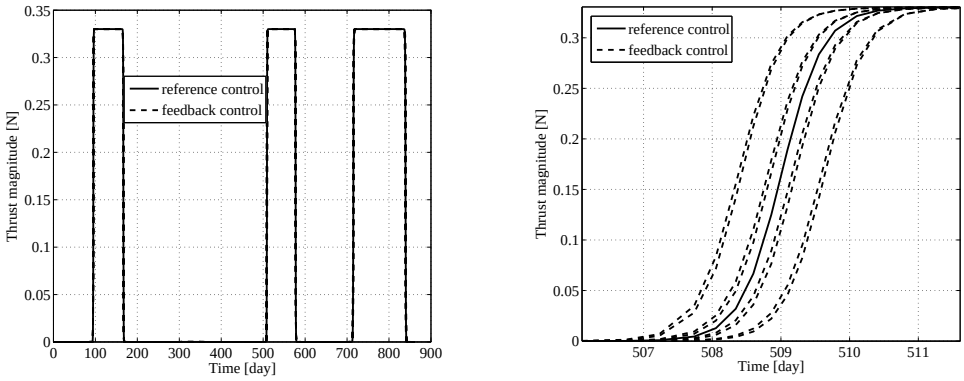

(a) Control profiles (b) Detail on third control switch

Figure 4.12: 3-bang Earth–1996 FG_3 transfer: optimal control profiles for perturbed final target positions.

The accuracy of the high order feedback is now investigated. First of all, the effect of the amplitude of the perturbation is studied. Referring to Figure 4.1, for increasing box amplitudes, the difference $\delta\tilde{\boldsymbol{r}}_f$ between the final position and the imposed perturbed final target position is computed. The maximum norm for all samples is reported in Figure 4.14(a). As expected, the

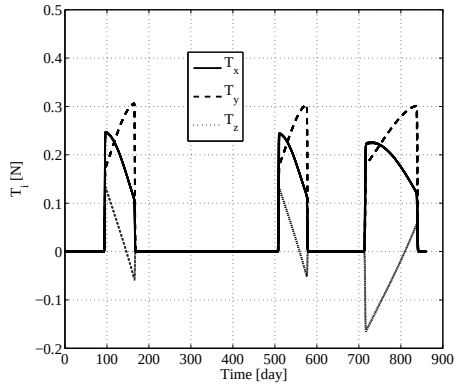

(a) Thrust components

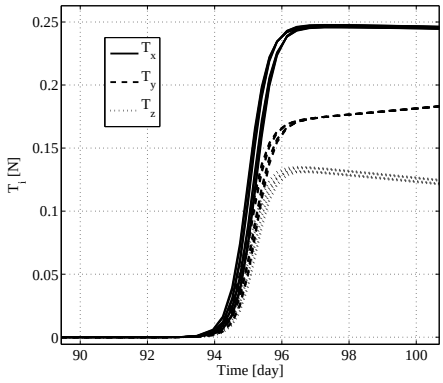

(b) Detail on first bang

Figure 4.13: 3-bang Earth–1996 FG_3 transfer: thrust components profiles for perturbed final target positions.

error increases with box amplitude. A comparison between Figure 4.14(a) and Figure 4.5(a) shows that the maximum error on the 3-bang reference trajectory is greater than that achieved on the 2-bang case. Nevertheless, the maps are still adequate to compute control corrections for boxes of amplitude up to 1E-3 AU, with a maximum error of about 1E-8 AU; i.e., five order of magnitude smaller than the perturbation.

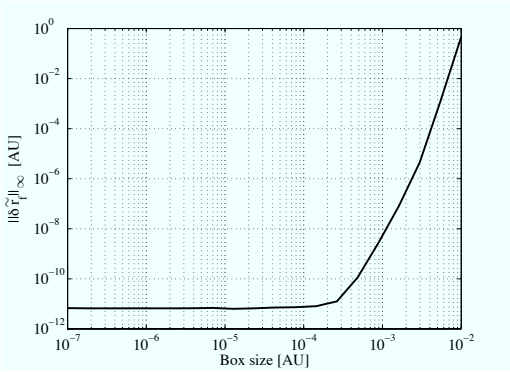

(a) Error vs. Box amplitude

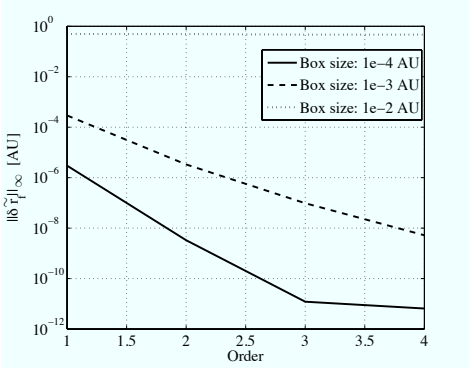

(b) Error vs. Order

Figure 4.14: 3-bang Earth–1996 FG_3 transfer: accuracy analysis for perturbed final target positions.

The improvement of the accuracy of the Taylor expansions for increasing order is studied in Figure 4.14(b). The trend of $\delta\tilde{\boldsymbol{r}}_f$ is reported in figure for increasing expansion orders and different error box amplitudes. Similarly to

the 2-bang test case, the accuracy of the maps increases with order for box amplitudes up to 1E-3 AU, whereas an irregular trend can be identified for the amplitude of 1E-2 AU.

Finally, the polynomial maps (4.8) and (4.9) are computed for the 3-bang Earth–1996 FG_3 reference solution under analysis. Thus, the LDB polynomial bounder is used to compute the propellant margins for different error box amplitudes and the results are reported in Table 4.4.

Table 4.4: 3-bang Earth–1996 FG_3 transfer: propellant margins for the perturbed final spacecraft position test case.

Reference m_p: 200.887 kg		
Box amplitude [AU]	m_p range [kg]	Margin [%]
1E-5	[200.878, 200.896]	0.004
1E-4	[200.797, 200.978]	0.045
1E-3	[199.983, 201.798]	0.453

4.3.2 Perturbed initial spacecraft position

The initial position is now supposed to be affected by measurable errors. For any error $\delta \boldsymbol{r}_0$, the polynomial map (4.6) is evaluated at $\delta \boldsymbol{x}_0 = [\delta \boldsymbol{r}_0, 0]$ and $\delta \boldsymbol{x}_f = [0, 0]$ to compute the optimal correction to the initial costates. The new values of $\boldsymbol{\lambda}_{x_0}$ and λ_{m_0} supplies the optimal control to reach the reference position of 1996 FG_3 at t_f from the perturbed initial position.

The performances of the algorithm are first assessed for a maximum error of 1E-3 AU on each component of the initial spacecraft position. The corners of the associated cube are sampled and the corresponding optimal transfers are computed by evaluating the map (4.6) and integrating the ODEs (3.1). Similarly to the previous test cases, for each sample, the maximum norm between the resulting trajectories and the reference trajectory is reported in Figure 4.15. The initial error of 1E-3 AU is reduced along the transfer and canceled at t_f.

The resulting optimal control magnitude profiles and a detail on the first steep increase of the control action are plotted in Figure 4.16(a) and Figure 4.16(b) respectively. Once again, the effect of perturbations on the initial spacecraft position is greater than for the case of perturbed final positions, and the optimal switching time for the sampled trajectories varies within a range of about 2 days. The thrust components profiles corresponding to each sample are reported in Figure 4.17(a), whereas a detail of the first bang is reported in Figure 4.17(b).

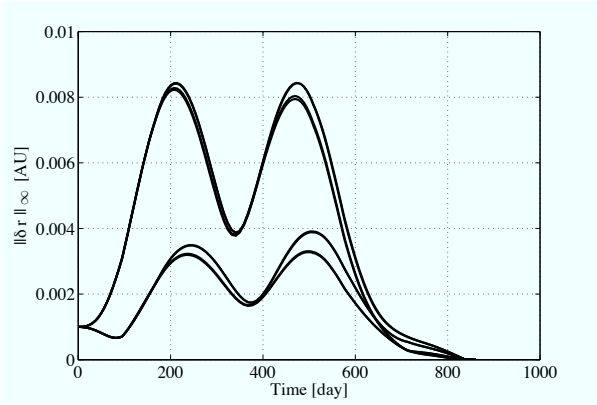

Figure 4.15: 3-bang Earth–1996 FG_3 transfer: optimal feedback on perturbed initial spacecraft positions. Trajectory displacement along the transfer.

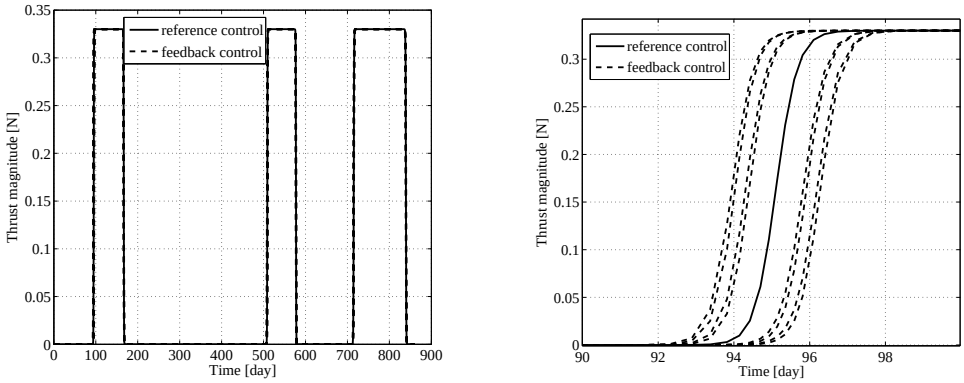

(a) Control profiles

(b) Detail on first control switch

Figure 4.16: 3-bang Earth–1996 FG_3 transfer: optimal control profiles for perturbed initial spacecraft positions.

The accuracy of the fourth order maps (4.6) is investigated by computing the final position error $\delta \boldsymbol{r}_f$ with respect to the target. The maximum norm over all the samples for different box amplitudes is reported in Figure 4.18(a). The error increases with box amplitude. The results are comparable with those achieved for the 2-bang test case: the maps are sufficiently accurate to compute control corrections for error boxes of amplitude up to 1E-3 AU.

Similarly to the previous test cases, the polynomial maps (4.8) and (4.9) of the 3-bang transfer are bounded for different error box amplitudes on the initial spacecraft position to compute propellant margins. The results are reported in Table 4.5.

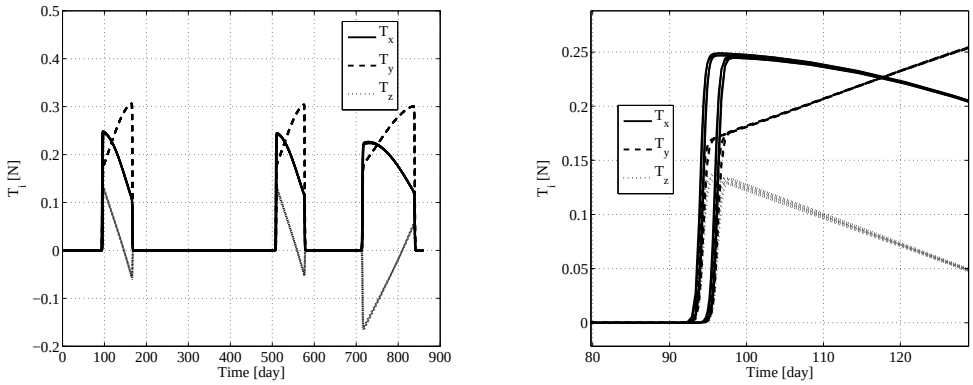

(a) Thrust components (b) Detail on first bang

Figure 4.17: 3-bang Earth–1996 FG_3 transfer: thrust components profiles for perturbed initial spacecraft positions.

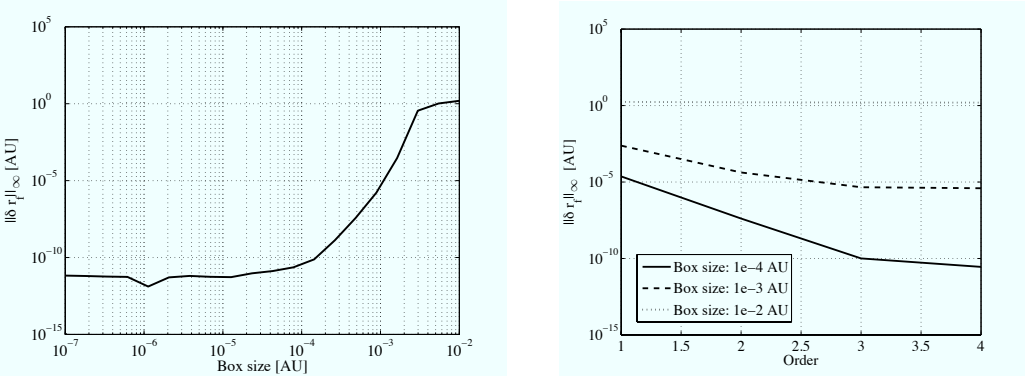

(a) Error vs. Box amplitude (b) Error vs. Order

Figure 4.18: 3-bang Earth–1996 FG_3 transfer. Accuracy analysis for perturbed initial spacecraft positions

Table 4.5: 3-bang Earth–1996 FG_3 transfer: propellant margins for the perturbed initial spacecraft position test case.

Reference m_p: 200.887 kg		
Box amplitude [AU]	m_p range [kg]	Margin [%]
1E-5	[200.877, 200.897]	0.005
1E-4	[200.786, 200.988]	0.050
1E-3	[199.894, 201.914]	0.511

4.4 Transfer to 1996 FG_3: 4-bang solution

The 4-bang trajectory to asteroid 1996 FG_3 reported in Section 3.2.3 is now used as reference solution. Fourth order maps (4.6) are computed using the algorithm introduced in Section 4.1. The performances of the method are studied hereafter on perturbed final and initial positions.

4.4.1 Perturbed final target position

The case of measurable errors on the final position of asteroid 1996 FG_3 is addressed in this section. Given any final position error $\delta\boldsymbol{r}_f$, the polynomial map (4.6) is evaluated by setting $\delta\boldsymbol{x}_0 \equiv [\delta\boldsymbol{r}_0, \delta\boldsymbol{v}_0] = [0, 0]$ and $\delta\boldsymbol{x}_f \equiv [\delta\boldsymbol{r}_f, \delta\boldsymbol{v}_f] = [\delta\boldsymbol{r}_f, 0]$. The new optimal values of the initial costates are then computed, which deliver the optimal control corrections to transfer the spacecraft from the reference initial state to the perturbed final target position.

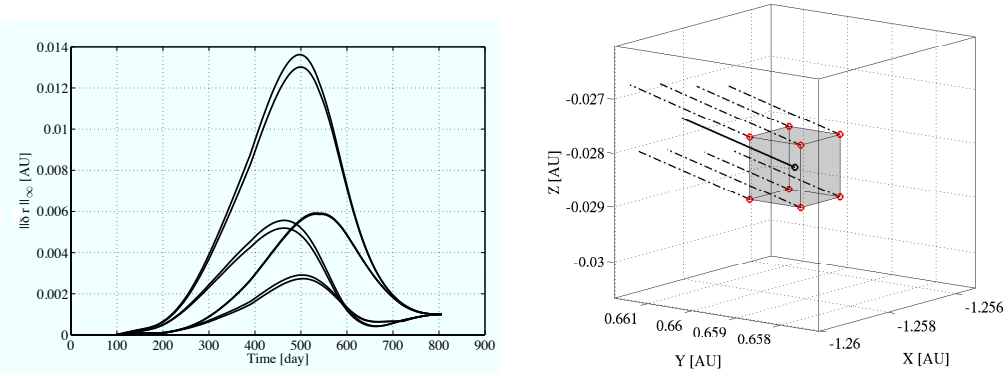

(a) Displacement along the transfer

(b) Detail at arrival

Figure 4.19: 4-bang Earth–1996 FG_3 transfer: optimal feedback on perturbed final target positions.

The case of a maximum perturbation of 1E-3 AU on each component of the final target position is first investigated. For each corner of the corresponding cube, the associated $\delta\boldsymbol{r}_f$ is computed and the map (4.6) is evaluated to obtain the new optimal transfer trajectory. The resulting maximum norm of the difference between the resulting trajectory and the reference trajectory is reported in Figure 4.19(a). Similarly to the previous test cases, the fourth order corrections guide the spacecraft from the reference initial state to the final imposed offset of 1E-3 AU. A detail of all trajectories at arrival is reported in Figure 4.19(b).

Figure 4.20(a) plots the resulting optimal control magnitude profiles and Figure 4.20(b) reports a detail at the beginning of the last propelled arc, which shows the largest variation on the switching time. Compared to the 2-bang and 3-bang test cases, the 4-bang solution is characterized by a slightly larger range for the switching times, reaching a maximum of about 2 days. For the sake of completeness, the feedback on the thrust direction is investigated in Figure 4.21(a). The profiles of the components of the thrust vector are illustrated and a detail of the last bang is reported in Figure 4.21(b).

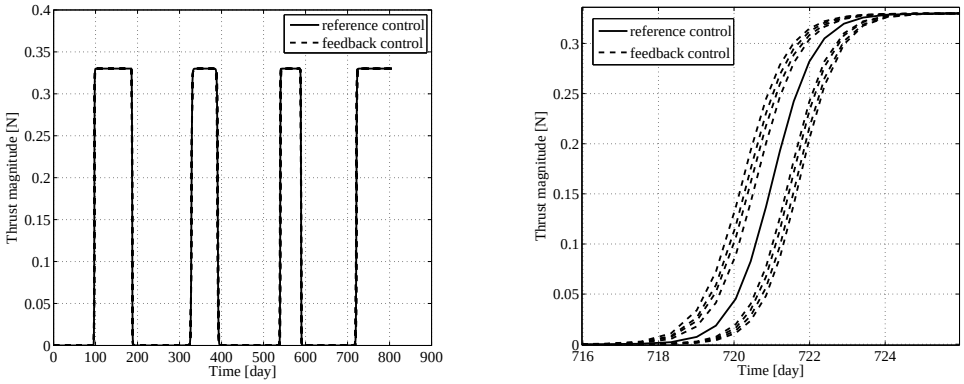

(a) Control profiles (b) Detail on last control switch

Figure 4.20: 4-bang Earth–1996 FG_3 transfer: optimal control profiles for perturbed final target positions.

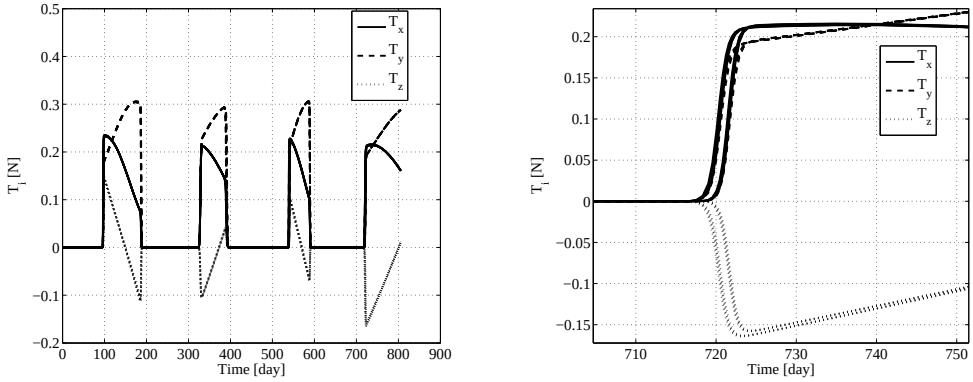

(a) Thrust components (b) Detail on last bang

Figure 4.21: 4-bang Earth–1996 FG_3 transfer: thrust components profiles for perturbed final target positions.

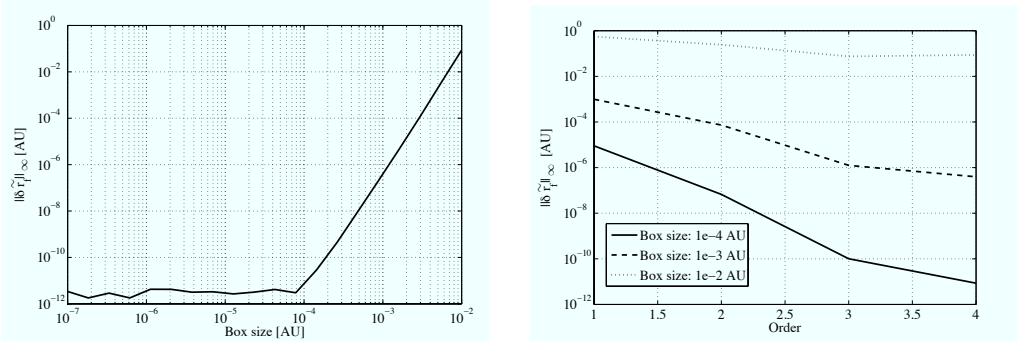

(a) Error vs. Box amplitude (b) Error vs. Order

Figure 4.22: 4-bang Earth–1996 FG_3 transfer: accuracy analysis for perturbed final target positions.

The performances of the method for different error box amplitudes are studied in Figure 4.22(a). More specifically, referring again to Figure 4.1, for increasing box amplitudes, the difference $\delta\tilde{\boldsymbol{r}}_f$ between the final position and the imposed perturbed final target position is computed. The maximum norm for all samples is reported in the figure. By comparing Figure 4.22(a) with Figure 4.14(a) and Figure 4.5(a), we can see that the maximum error for the 4-bang solution is evidently greater than those achieved in the 2-bang and 3-bang cases, especially for larger box amplitudes. In particular, the maximum error for a box amplitude of 1E-3 AU is about 1E-6 AU; i.e., two orders of magnitude greater than in the other test cases. Nevertheless, it is still limited to 0.1% of the imposed perturbation.

The behaviour of the final position maximum error with respect to order and box size is plotted in Figure 4.22(b). The trend is similar to those in Figures 4.5(b) and 4.14(b), with an increasing accuracy with the order of expansion. Similarly to the 3-bang case the box amplitude of 1E-2 AU provides an error which is larger than the imposed perturbation.

Finally, the propellant margins are assessed by computing the polynomial maps (4.8) and (4.9) for the 4-bang Earth–1996 FG_3 reference solution under analysis. The LDB polynomial bounder is used to bound the resulting maps for different error box amplitudes. The results are reported in Table 4.6.

4.4.2 Perturbed initial spacecraft position

The case of perturbed initial position is studied in this section. For any error $\delta\boldsymbol{r}_0$, the polynomial map (4.6) is evaluated at $\delta\boldsymbol{x}_0 = [\delta\boldsymbol{r}_0, 0]$ and $\delta\boldsymbol{x}_f = [0, 0]$. The associated values of $\boldsymbol{\lambda}_{x_0}$ and λ_{m_0} supplies the optimal control to reach

Table 4.6: 4-bang Earth–1996 FG_3 transfer: propellant margins for the perturbed final spacecraft position test case.

Reference m_p: 217.834 kg		
Box amplitude [AU]	m_p range [kg]	Margin [%]
1E-5	[217.826, 217.842]	0.004
1E-4	[217.754, 217.913]	0.036
1E-3	[217.043, 218.638]	0.369

the reference position of 1996 FG_3 at t_f from the perturbed initial position.

A maximum perturbation of 1E-3 AU is set on each component of the initial spacecraft position to study feedback performances. The corners of the associated cube are sampled and the corresponding optimal transfers are computed by evaluating the map (4.6). Figure 4.23 reports the profiles of the position displacement with respect to the reference trajectory for each corner of the initial error box. Similarly to the other test cases, the displacement is supplied in terms of the maximum norm between the resulting trajectories and the reference trajectory. The initial error of 1E-3 AU is reduced along the transfer and canceled at t_f.

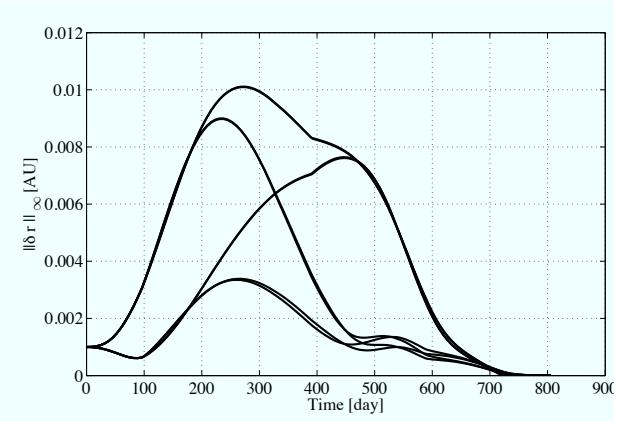

Figure 4.23: 4-bang Earth–1996 FG_3 transfer: optimal feedback on perturbed initial spacecraft positions. Trajectory displacement along the transfer.

The associated variation of the optimal control switching times is illustrated in Figure 4.24(a). A detail of the switch at the beginning of the last bang is reported in Figure 4.24(b), which shows that the maximum variation of the switching times is of the order of 2 days. The thrust components profiles corresponding to each sample are reported in Figure 4.25(a), whereas a detail of the second bang is reported in Figure 4.25(b).

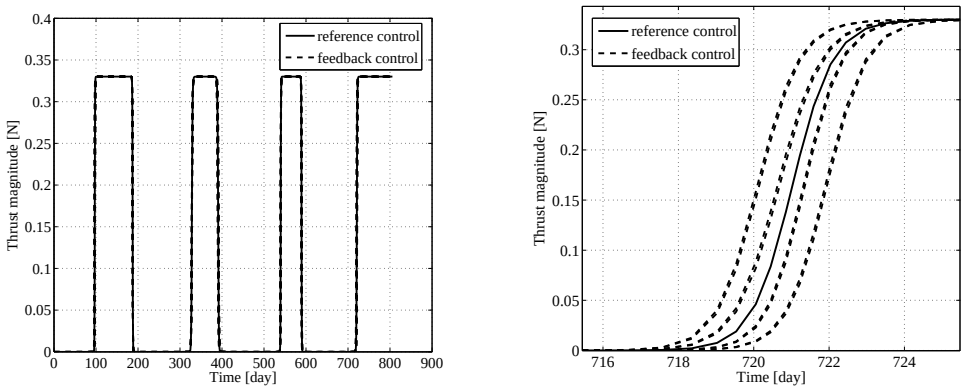

(a) Control profiles (b) Detail on third control switch

Figure 4.24: 4-bang Earth–1996 FG_3 transfer: optimal control profiles for perturbed initial spacecraft positions.

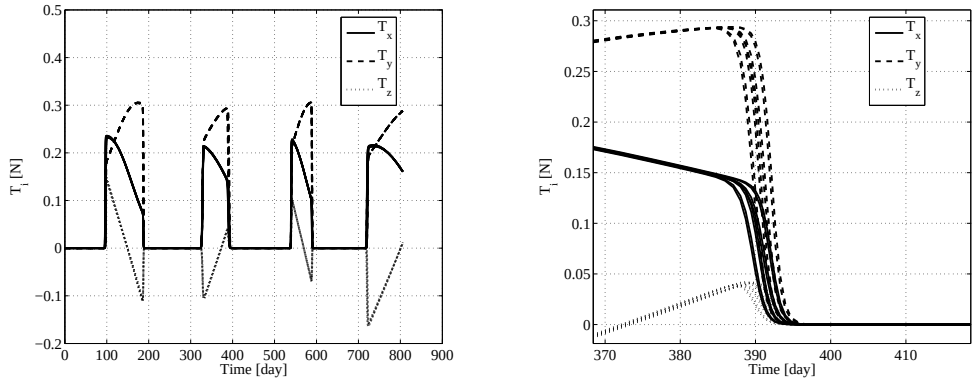

(a) Thrust components (b) Detail on second bang

Figure 4.25: 3-bang Earth–1996 FG_3 transfer: thrust components profiles for perturbed initial spacecraft positions.

The trend of the error of the fourth order Taylor expansion for different box amplitudes is investigated in Figure 4.26(a). More specifically, the maximum norm of the final position error with respect to the target over all the samples, $\|\delta \boldsymbol{r}_f\|_\infty$, is plotted. The error increases with box size and, in particular, is four order of magnitude smaller than the perturbation for an error box of 1E-3 AU.

According to Figure 4.26(b), the fourth order expansion is sufficiently accurate to compute control corrections for box amplitudes up to 1E-3 AU

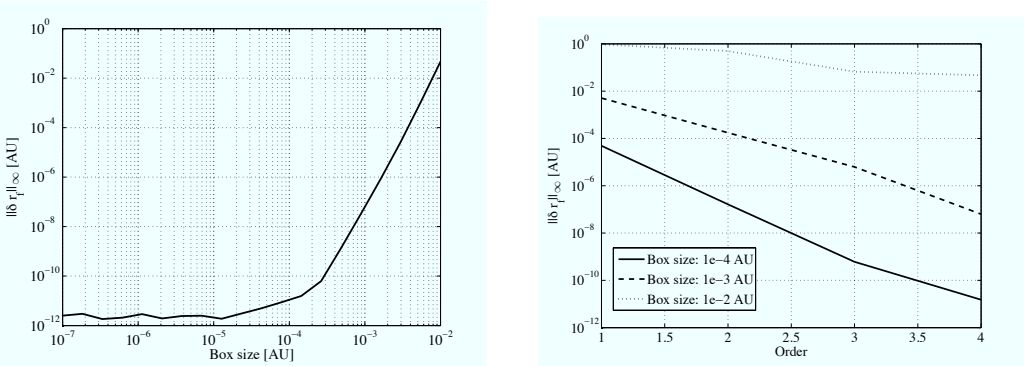

(a) Error vs. Box amplitude

(b) Error vs. Order

Figure 4.26: 4-bang Earth–1996 FG_3 transfer. Accuracy analysis for perturbed initial spacecraft positions

(for amplitude of 1E-3 AU, a third order expansion guarantees an error of 1E-5 AU).

Similarly to the previous test cases, the polynomial maps (4.8) and (4.9) of the 4-bang transfer are bounded for different error box amplitudes on the initial spacecraft position to compute propellant margins. The results are reported in Table 4.7.

Table 4.7: 4-bang Earth–1996 FG_3 transfer: propellant margins for the perturbed initial spacecraft position test case.

Reference m_p: 217.834 kg		
Box amplitude [AU]	m_p range [kg]	Margin [%]
1E-5	[217.823, 217.845]	0.005
1E-4	[217.724, 217.943]	0.050
1E-3	[216.754, 218.947]	0.511

Chapter 5

High order expansion of the fuel-optimal bang-bang solution

Following the approach presented in Chapter 4, the algorithm for the high order expansion of the exact bang-bang solution of the fuel-optimal control problem about a reference trajectory is introduced in this chapter. More specifically, the limits associated to the $\mathcal{C}^\infty$ approximation of the solution are removed: the discontinuous solution obtained at the end of the three-step procedure reported in Section 3.1.1 is used as reference trajectory; then, an algorithm for its high order expansion with respect to boundary conditions is presented, which solves the discontinuity by managing the expansion of the switching times. The performances of the algorithm are assessed on the transfer to asteroid 1996 FG_3, considering different reference solutions with increasing transfer time and number of bangs. The accuracy of the expansions are provided and its limits discussed.

5.1 DA algorithm for the fuel-optimal bang-bang solution

Assume a reference solution of the FOP (3.1)-(3.3) is available. Thus, the initial costates, $\boldsymbol{\lambda}_{x_0} = [\boldsymbol{\lambda}_{r_0}, \boldsymbol{\lambda}_{v_0}]$ and λ_{m_0}, the final costates, $\boldsymbol{\lambda}_{x_f} = \left[\boldsymbol{\lambda}_{r_f}, \boldsymbol{\lambda}_{v_f}\right]$ and λ_{m_f}, and the control switching times t_{s_i}, $i = 1, \ldots, q$, have been computed for assigned initial conditions, $\boldsymbol{x_0} = [\boldsymbol{r}_0, \boldsymbol{v}_0]$ and m_0, and final target position and velocity $\boldsymbol{x_f} = [\boldsymbol{r}_f, \boldsymbol{v}_f]$. It is worth recalling that $\lambda_{m_f} = 0$ for the transversality condition. The DA algorithm for the arbitrary order expansion of the exact bang-bang solution of the FOP with respect to both the initial spacecraft state and the final target state is based on the following steps.

Step 1. Initialize the initial spacecraft state, the initial costates, and the first control switching time as DA variables. This means the variations with respect to their reference values are considered:

$$\begin{aligned} [\boldsymbol{x}_0] &= \boldsymbol{x}_0 + \delta\boldsymbol{x}_0 \\ [\boldsymbol{\lambda}_{x_0}] &= \boldsymbol{\lambda}_{x_0} + \delta\boldsymbol{\lambda}_{x_0} \\ [\lambda_{m_0}] &= \lambda_{m_0} + \delta\lambda_{m_0} \\ [t_{s_1}] &= t_{s_1} + \delta t_{s_1}. \end{aligned} \tag{5.1}$$

Step 2. Using the techniques introduced in Section 2.2, perform a DA-based integration of the ODEs (3.1) and (3.8) from t_0 to $[t_{s_1}]$ to obtain the high order expansion of the flow at $[t_{s_1}]$. More specifically, the dependence of the spacecraft state, mass, and costates on the perturbed initial conditions and δt_{s_1} is obtained in terms of the high order polynomial map

$$\begin{pmatrix} [\boldsymbol{x}_1] \\ [m_1] \\ [\boldsymbol{\lambda}_{x_1}] \\ [\lambda_{m_1}] \end{pmatrix} = \begin{pmatrix} \boldsymbol{x}_1 \\ m_1 \\ \boldsymbol{\lambda}_{x_1} \\ \lambda_{m_1} \end{pmatrix} + \begin{pmatrix} \mathcal{M}_{\boldsymbol{x}_1} \\ \mathcal{M}_{m_1} \\ \mathcal{M}_{\boldsymbol{\lambda}_{x_1}} \\ \mathcal{M}_{\lambda_{m_1}} \end{pmatrix} \begin{pmatrix} \delta\boldsymbol{x}_0 \\ \delta\boldsymbol{\lambda}_{x_0} \\ \delta\lambda_{m_0} \\ \delta t_{s_1} \end{pmatrix}, \tag{5.2}$$

where $\mathcal{M}_{\boldsymbol{x}_1}$, $\mathcal{M}_{m_1}$, $\mathcal{M}_{\boldsymbol{\lambda}_{x_1}}$, and $\mathcal{M}_{\lambda_{m_1}}$ denote high order polynomials in $\delta\boldsymbol{x}_0$, $\delta\boldsymbol{\lambda}_{x_0}$, $\delta\lambda_{m_0}$, and δt_{s_1}.

Step 3. Compute the switching function (3.7) in the DA framework, which yields the Taylor polynomial

$$[\rho_1] = \delta\rho_1 = 1 - \frac{I_{sp} g_0 \, [\lambda_{v1}]}{[m_1]} - [\lambda_{m_1}] = \mathcal{M}_{\rho_1}(\delta\boldsymbol{x}_0, \delta\boldsymbol{\lambda}_{x_0}, \delta\lambda_{m_0}, \delta t_{s_1}). \tag{5.3}$$

It is worth observing that the constant part of map (5.3) is the value of the switching function at t_{s_1} corresponding to the reference solution, which equals zero. Thus, $[\rho_1] = \delta\rho_1$.

Step 4. Consider the map

$$\begin{pmatrix} \delta\rho_1 \\ \delta\boldsymbol{x}_0 \\ \delta\boldsymbol{\lambda}_{x_0} \\ \delta\lambda_{m_0} \end{pmatrix} = \begin{pmatrix} \mathcal{M}_{\rho_1} \\ \mathcal{I}_{\boldsymbol{x}_0} \\ \mathcal{I}_{\boldsymbol{\lambda}_{x_0}} \\ \mathcal{I}_{\lambda_{m_0}} \end{pmatrix} \begin{pmatrix} \delta\boldsymbol{x}_0 \\ \delta\boldsymbol{\lambda}_{x_0} \\ \delta\lambda_{m_0} \\ \delta t_{s_1} \end{pmatrix}, \tag{5.4}$$

which is built by concatenating map (5.3) with the identity maps for $\delta\boldsymbol{x}_0$, $\delta\boldsymbol{\lambda}_{x_0}$, and $\delta\lambda_{m_0}$.

Step 5. Invert the above map to obtain

$$\begin{pmatrix} \delta\boldsymbol{x}_0 \\ \delta\boldsymbol{\lambda}_{x_0} \\ \delta\lambda_{m_0} \\ \delta t_{s_1} \end{pmatrix} = \begin{pmatrix} \mathcal{M}_{\rho_1} \\ \mathcal{I}_{\boldsymbol{x}_0} \\ \mathcal{I}_{\boldsymbol{\lambda}_{x_0}} \\ \mathcal{I}_{\lambda_{m_0}} \end{pmatrix}^{-1} \begin{pmatrix} \delta\rho_1 \\ \delta\boldsymbol{x}_0 \\ \delta\boldsymbol{\lambda}_{x_0} \\ \delta\lambda_{m_0} \end{pmatrix}. \tag{5.5}$$

This is the inversion of high order polynomials, which can be readily performed by reducing the inversion problem to an equivalent fixed-point problem as described in [6]. The fourth component of map (5.5) relates the first control switching time to the deviation $\delta\rho_1$ of the switching function from its reference value $\rho_1 = 0$, and the perturbations $\delta\boldsymbol{x}_0$, $\delta\boldsymbol{\lambda}_{x_0}$, and $\delta\lambda_{m_0}$.

Step 6. Given any $\delta\boldsymbol{x}_0$, $\delta\boldsymbol{\lambda}_{x_0}$, and $\delta\lambda_{m_0}$, we can compute the corresponding switching time by imposing $\delta\rho_1 = 0$ in Eq. (5.5),

$$\begin{pmatrix} \delta\boldsymbol{x}_0 \\ \delta\boldsymbol{\lambda}_{x_0} \\ \delta\lambda_{m_0} \\ \delta t_{s_1} \end{pmatrix} = \begin{pmatrix} \mathcal{M}_{\rho_1} \\ \mathcal{I}_{\boldsymbol{x}_0} \\ \mathcal{I}_{\boldsymbol{\lambda}_{x_0}} \\ \mathcal{I}_{\lambda_{m_0}} \end{pmatrix}^{-1} \begin{pmatrix} 0 \\ \delta\boldsymbol{x}_0 \\ \delta\boldsymbol{\lambda}_{x_0} \\ \delta\lambda_{m_0} \end{pmatrix}. \tag{5.6}$$

Let us extract the fourth component of (5.6), which will be indicated as

$$\delta t_{s_1} = \mathcal{M}_{\rho_1=0}(\delta\boldsymbol{x}_0, \delta\boldsymbol{\lambda}_{x_0}, \delta\lambda_{m_0}). \tag{5.7}$$

The map (5.7) can be added to the reference t_{s_1} to obtain the Taylor polynomial

$$[t_{s_1}]_{\rho_1=0} = t_{s_1} + \delta t_{s_1} = t_{s_1} + \mathcal{M}_{\rho_1=0}(\delta\boldsymbol{x}_0, \delta\boldsymbol{\lambda}_{x_0}, \delta\lambda_{m_0}), \tag{5.8}$$

which is the Taylor expansion of the constraint manifold $\rho_1 = 0$; i.e., the Taylor expansion of the first switching time with respect to the perturbations on the initial conditions.

Step 7. Compose map (5.2) with (5.6) to obtain the Taylor expansion of the spacecraft state and costate at the first control switch with respect to the initial conditions,

$$\begin{pmatrix} [\boldsymbol{x}_1] \\ [m_1] \\ [\boldsymbol{\lambda}_{x_1}] \\ [\lambda_{m_1}] \end{pmatrix}_{\rho_1=0} = \begin{pmatrix} \boldsymbol{x}_1 \\ m_1 \\ \boldsymbol{\lambda}_{x_1} \\ \lambda_{m_1} \end{pmatrix} + \begin{pmatrix} \mathcal{M}_{\boldsymbol{x}_1} \\ \mathcal{M}_{m_1} \\ \mathcal{M}_{\boldsymbol{\lambda}_{x_1}} \\ \mathcal{M}_{\lambda_{m_1}} \end{pmatrix}_{\rho_1=0} \begin{pmatrix} \delta\boldsymbol{x}_0 \\ \delta\boldsymbol{\lambda}_{x_0} \\ \delta\lambda_{m_0} \end{pmatrix}. \tag{5.9}$$

The switching time t_{s_2} can now be initialized as a DA variable, $[t_{s_2}] = t_{s_2} + \delta t_{s_2}$, and steps 2 through 7 can be repeated from $[t_{s_1}]_{\rho_1=0}$ to $[t_{s_2}]$. By iterating the same procedure till t_{s_q} we obtain

$$[t_{s_q}]_{\boldsymbol{\rho}=0} = t_{s_q} + \mathcal{M}_{\boldsymbol{\rho}=0}(\delta\boldsymbol{x}_0, \delta\boldsymbol{\lambda}_{x_0}, \delta\lambda_{m_0}), \tag{5.10}$$

and

$$\begin{pmatrix} [\boldsymbol{x}_q] \\ [m_q] \\ [\boldsymbol{\lambda}_{x_q}] \\ [\lambda_{m_q}] \end{pmatrix}_{\boldsymbol{\rho}=0} = \begin{pmatrix} \boldsymbol{x}_q \\ m_q \\ \boldsymbol{\lambda}_{x_q} \\ \lambda_{m_q} \end{pmatrix} + \begin{pmatrix} \mathcal{M}_{\boldsymbol{x}_q} \\ \mathcal{M}_{m_q} \\ \mathcal{M}_{\boldsymbol{\lambda}_{x_q}} \\ \mathcal{M}_{\lambda_{m_q}} \end{pmatrix}_{\boldsymbol{\rho}=0} \begin{pmatrix} \delta\boldsymbol{x}_0 \\ \delta\boldsymbol{\lambda}_{x_0} \\ \delta\lambda_{m_0} \end{pmatrix} \tag{5.11}$$

where $\boldsymbol{\rho} = [\rho_1, \ldots, \rho_q]$.

Step 8. A DA-based integration is now performed from $[t_{s_q}]_{\boldsymbol{\rho}=0}$ to t_f. The resulting polynomial map

$$\begin{pmatrix} [\boldsymbol{x}_f] \\ [m_f] \\ [\boldsymbol{\lambda}_{x_f}] \\ [\lambda_{m_f}] \end{pmatrix}_{\boldsymbol{\rho}=0} = \begin{pmatrix} \boldsymbol{x}_f \\ m_f \\ \boldsymbol{\lambda}_{x_f} \\ \lambda_{m_f} \end{pmatrix} + \begin{pmatrix} \mathcal{M}_{\boldsymbol{x}_f} \\ \mathcal{M}_{m_f} \\ \mathcal{M}_{\boldsymbol{\lambda}_{x_f}} \\ \mathcal{M}_{\lambda_{m_f}} \end{pmatrix}_{\boldsymbol{\rho}=0} \begin{pmatrix} \delta\boldsymbol{x}_0 \\ \delta\boldsymbol{\lambda}_{x_0} \\ \delta\lambda_{m_0} \end{pmatrix} \tag{5.12}$$

is the Taylor approximation of the deviation of the final conditions from their reference values caused by the perturbed initial conditions and embedding the satisfaction of $\delta\rho_i = 0$, $i = 1, \ldots, q$.

Step 9. Extract the first and last components of (5.12), subtract their constant parts, and build the following map

$$\begin{pmatrix} \delta\boldsymbol{x}_0 \\ \delta\boldsymbol{x}_f \\ \delta\lambda_{m_f} \end{pmatrix} = \begin{pmatrix} \mathcal{I}_{\boldsymbol{x}_0} \\ \mathcal{M}_{\boldsymbol{x}_f} \\ \mathcal{M}_{\lambda_{m_f}} \end{pmatrix}_{\boldsymbol{\rho}=0} \begin{pmatrix} \delta\boldsymbol{x}_0 \\ \delta\boldsymbol{\lambda}_{x_0} \\ \delta\lambda_{m_0} \end{pmatrix}, \tag{5.13}$$

which includes the identity map on $\delta\boldsymbol{x}_0$.

Step 10. Invert map (5.13) and impose the transversality condition by setting $\delta\lambda_{m_f} = 0$. This yields

$$\begin{pmatrix} \delta\boldsymbol{x}_0 \\ \delta\boldsymbol{\lambda}_{x_0} \\ \delta\lambda_{m_0} \end{pmatrix} = \begin{pmatrix} \mathcal{I}_{\boldsymbol{x}_0} \\ \mathcal{M}_{\boldsymbol{x}_f} \\ \mathcal{M}_{\lambda_{m_f}} \end{pmatrix}^{-1}_{\boldsymbol{\rho}=0} \begin{pmatrix} \delta\boldsymbol{x}_0 \\ \delta\boldsymbol{x}_f \\ 0 \end{pmatrix}. \tag{5.14}$$

Step 11. Add the reference initial costates to the last two components of (5.14),

$$\begin{pmatrix} [\boldsymbol{\lambda}_{x_0}] \\ [\lambda_{m_0}] \end{pmatrix}_{\boldsymbol{\rho},\lambda_{m_f}=0} = \begin{pmatrix} \boldsymbol{\lambda}_{x_0} \\ \lambda_{m_0} \end{pmatrix} + \begin{pmatrix} \mathcal{M}_{\boldsymbol{\lambda}_{x_0}} \\ \mathcal{M}_{\lambda_{m_0}} \end{pmatrix}_{\boldsymbol{\rho},\lambda_{m_f}=0} \begin{pmatrix} \delta\boldsymbol{x}_0 \\ \delta\boldsymbol{x}_f \end{pmatrix} \tag{5.15}$$

and compose map (5.8) and its counterparts for the subsequent switching times with (5.14) to obtain

$$[t_{s_i}]_{\boldsymbol{\rho},\lambda_{m_f}=0} = t_{s_i} + (\mathcal{M}_{t_{s_i}})_{\boldsymbol{\rho},\lambda_{m_f}=0}(\delta\boldsymbol{x}_0, \delta\boldsymbol{x}_f) \tag{5.16}$$

for $i = 1, \ldots, q$. Together, maps (5.15) and (5.16) identify the high order Taylor expansion of the solution of the optimal control problem with respect to the initial spacecraft state and the final target state. More specifically, for any $\delta\boldsymbol{x}_0$ and $\delta\boldsymbol{x}_f$, the mere evaluation of the polynomial map (5.15) delivers the associated optimal costates. In addition, the polynomials (5.16) can be evaluated to identify the corresponding optimal control switching times. It is worth observing that the polynomial maps (5.15) and (5.16) supply high order Taylor approximations of the solution of the optimal control problem for perturbed initial and final conditions, which are accurate up to the order used for the DA-based computation.

5.2 Transfer to 1996 FG_3: 2-bang solution

The performances of the algorithm introduced in the previous section are assessed on the Earth-1996 FG_3 transfer. The 2-bang reference trajectory reported in Section 3.2.1 is analyzed in this section. More specifically, the fuel optimal transfer trajectory and control profile reported in Figures 3.1(a) and 3.1(c) are used as reference solution for the Taylor expansions. The algorithm is then applied to compute a fourth order Taylor expansion of the solution of the FOP about the reference trajectory. Thus, the resulting maps (5.15) and (5.16) are fourth order polynomials in $\delta\boldsymbol{x}_0$ and $\delta\boldsymbol{x}_f$. The case of perturbed final target position is first investigated. The analysis for perturbed initial spacecraft position follows.

5.2.1 Perturbed final target position

The final position of asteroid 1996 FG_3, $\boldsymbol{r}_f$, is supposed to be affected by measurable errors. Given any displacement $\delta\boldsymbol{r}_f$ of the final target position from its reference value, the polynomial map (5.15) is evaluated by setting $\delta\boldsymbol{x}_0 \equiv [\delta\boldsymbol{r}_0, \delta\boldsymbol{v}_0] = [0, 0]$ and $\delta\boldsymbol{x}_f \equiv [\delta\boldsymbol{r}_f, \delta\boldsymbol{v}_f] = [\delta\boldsymbol{r}_f, 0]$. The corresponding

optimal values of $\boldsymbol{\lambda}_{x_0}$ and λ_{m_0} are computed. Then, starting from the reference initial spacecraft state and the new initial costates, a forward point-wise integration of the ODEs (3.1) and (3.8) supplies the optimal control law to transfer the spacecraft from the reference initial state to the perturbed final target position $\tilde{\boldsymbol{r}}_f = \boldsymbol{r}_f + \delta\boldsymbol{r}_f$. Moreover, map (5.16) is evaluated to identify the optimal control switching times of the new trajectory.

The performances of the procedure are studied hereafter. A maximum position error of 1E-3 AU affects each component of the final target state. For each corner of the corresponding cube, the associated $\delta\boldsymbol{r}_f$ is computed and the map (5.15) is evaluated to obtain the new optimal transfer trajectory. For each sample, the maximum norm of the difference between the resulting trajectory $\tilde{\boldsymbol{r}}(t)$ and the reference trajectory $\boldsymbol{r}(t)$ is reported in Figure 5.1(a). Starting from the reference initial position, the new trajectories tend to move away from the reference along the transfer and reach the final imposed value of 1E-3 AU. A detail of all trajectories at arrival is reported in Figure 5.1(b). Thanks to the high order feedback, each new optimal trajectory reaches the corresponding perturbed target.

For each sample, map (5.16) is evaluated to obtain the corresponding optimal control switching times. Figure 5.2(a) plots the resulting optimal control magnitude profiles, whereas a detail on the last control switch is reported in Figure 5.2(b). The optimal switching time for the sampled trajectories varies within a range of about 2 days. Once again, it is worth highlighting that the computation of each optimal switching time is reduced to the evaluation of a polynomial. For the sake of completeness, the feedback on the thrust direction is investigated in Figure 5.3(a). For each sample, the profiles of the

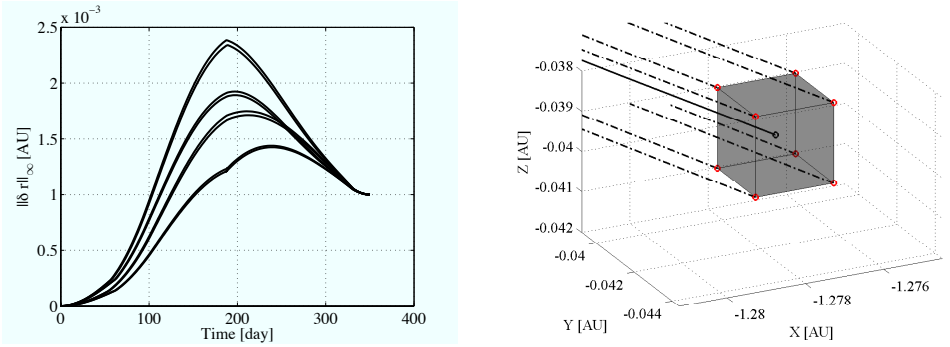

(a) Trajectory displacement along the transfer

(b) Detail at arrival

Figure 5.1: 2-bang Earth–1996 FG_3 transfer: optimal feedback on perturbed final target positions.

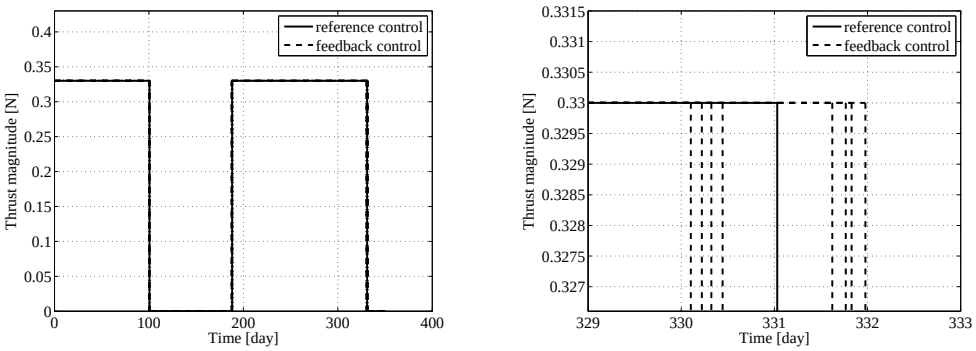

(a) Control profiles (b) Detail on last control switch

Figure 5.2: 2-bang Earth–1996 FG_3 transfer: optimal control profiles for perturbed final target positions.

components of the thrust vector are illustrated. A detail of the last bang is reported in Figure 5.3(b).

The accuracy of the fourth order maps (5.15) and (5.16) is investigated in Figure 5.5(a). More specifically, the difference $\delta\tilde{\boldsymbol{r}}_f$ between the final position and the desired perturbed final target position is computed (refer to Figure 5.4 for an illustration of the defined quantities). The maximum norm for all samples is then reported. The same process is repeated for different box amplitudes. As expected, the error increases with box amplitude, and the maps are not adequate to compute control corrections for error boxes of amplitude larger than 1E-3 AU, which is however well above the errors to be

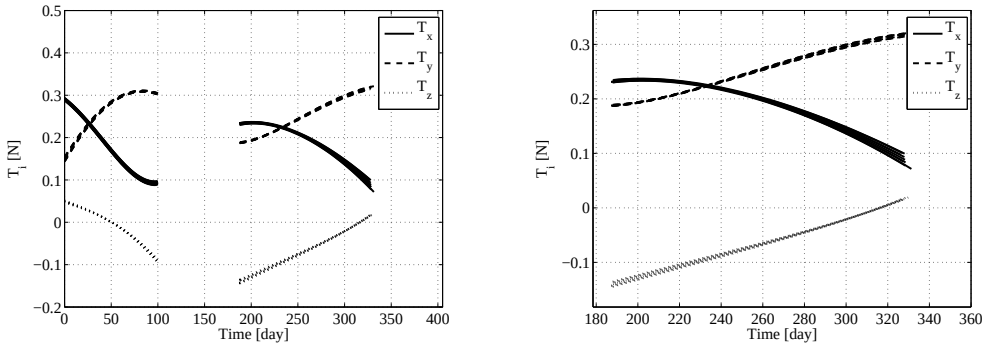

(a) Thrust components (b) Detail on last bang

Figure 5.3: 2-bang Earth–1996 FG_3 transfer: thrust components profiles for perturbed final target positions.

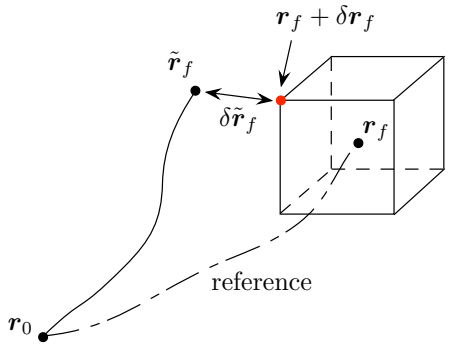

Figure 5.4: Illustration of the transfer to a perturbed final target position.

managed in practical applications.

The rationales about the inaccuracy of Taylor expansions for error boxes of amplitude larger than 1E-3 AU can be found in Figure 5.6(a) and Figure 5.6(b). More specifically, the two figures report the switching function profile for each sample and for box amplitudes of 1E-3 AU and 1E-2 AU, respectively. As can be seen from Figure 5.6(a), the variation of the switching function within the error box of 1E-3 AU is relatively small and does not break the overall structure of the bang–bang control profile (e.g., number of bangs and control switch location). This is not the case for a box amplitude of 1E-2 AU. Figure 5.6(b) shows that the switching function reaches zero at the end of the transfer for some samples, which warns of the appearance of a new switch. However, the algorithm presented in Section 5.1 works only

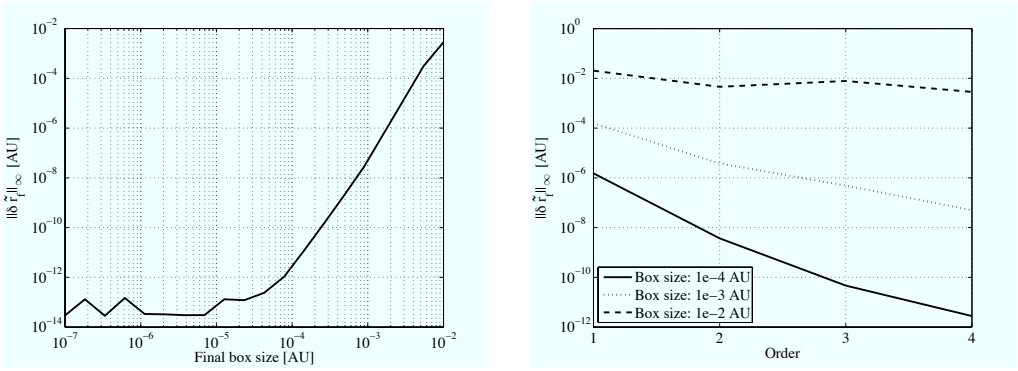

(a) Error vs. Box amplitude (b) Error vs. Order

Figure 5.5: 2-bang Earth–1996 FG_3 transfer: accuracy analysis for perturbed final target positions.

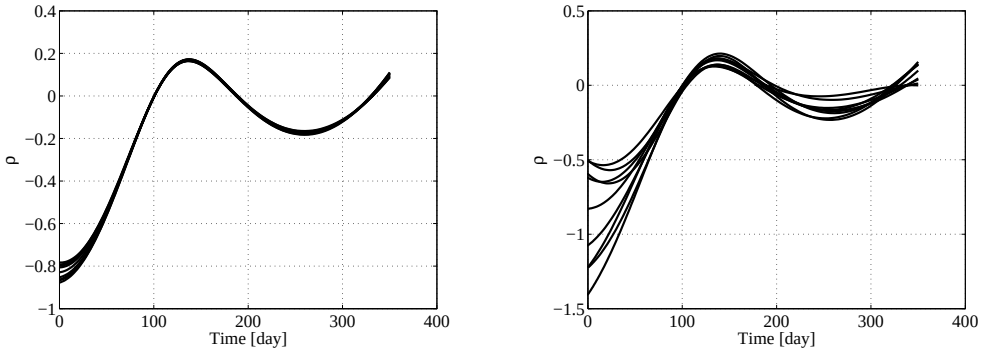

(a) Box amplitude: 10^{-3} AU (b) Box amplitude: 10^{-2} AU

Figure 5.6: 2-bang Earth–1996 FG_3 transfer: switching function for perturbed final target positions.

for a given structure of the bang–bang control profile: the appearance of additional control switches is a discontinuity that can not be handled by the Taylor expansion.

The effects of the order on the accuracy of the Taylor expansions is studied in Figure 5.5(b). The trend of $\delta\tilde{\boldsymbol{r}}_f$ is reported in figure for increasing expansion orders and different error box amplitudes. The accuracy of the maps increases with order for box amplitudes up to 1E-3 AU. An irregular trend is revealed instead for an amplitude of 1E-2 AU, which points out that convergence properties start to fail in the interval [1E-3, 1E-2] AU.

One of the main advantages of the DA-based algorithm of Section 5.1 lies in the availability of the functional dependency between the final spacecraft state and the perturbations, which can be profitably used to compute the propellant margins to compensate for the associated errors. More in detail, map (5.12) can be composed with map (5.14) to obtain

$$\begin{pmatrix} [\boldsymbol{x}_f] \\ [m_f] \\ [\boldsymbol{\lambda}_{x_f}] \\ [\lambda_{m_f}] \end{pmatrix}_{\boldsymbol{\rho},\lambda_{m_f}=0} = \begin{pmatrix} \boldsymbol{x}_f \\ m_f \\ \boldsymbol{\lambda}_{x_f} \\ \lambda_{m_f} \end{pmatrix} + \begin{pmatrix} \mathcal{M}_{\boldsymbol{x}_f} \\ \mathcal{M}_{m_f} \\ \mathcal{M}_{\boldsymbol{\lambda}_{x_f}} \\ \mathcal{M}_{\lambda_{m_f}} \end{pmatrix}_{\boldsymbol{\rho},\lambda_{m_f}=0} \begin{pmatrix} \delta\boldsymbol{x}_0 \\ \delta\boldsymbol{x}_f \end{pmatrix}. \tag{5.17}$$

Extract the second component of map (5.17):

$$[m_f]_{\boldsymbol{\rho},\lambda_{m_f}=0} = m_f + (\mathcal{M}_{m_f})_{\boldsymbol{\rho},\lambda_{m_f}=0}(\delta\boldsymbol{x}_0, \delta\boldsymbol{x}_f). \tag{5.18}$$

The polynomial (5.18) is the Taylor expansion of the optimal final spacecraft mass, i.e., for any perturbed initial and final state, the evaluation of map

(5.18) gives the final spacecraft mass when the optimal control law (5.15) is applied to the spacecraft. The resulting map for the 2-bang Earth–1996 FG_3 transfer with perturbed final position is reported in Table 5.1. Note that the Taylor polynomial in the table is obtained in the scaled vector $\delta \boldsymbol{r}_f^* = 1\text{E-}4\,\delta \boldsymbol{r}_f$ to favor the floating point representation of the coefficients.

Similarly to Chapter 4, the LDB polynomial bounder is applied on map (5.18) to compute propellant margins. First of all, the Taylor expansion of the propellant mass with respect to the perturbed initial and final states is computed. This can be achieved by subtracting (5.18) to the initial spacecraft wet mass m_0 for

$$[m_p]_{\boldsymbol{\rho},\lambda_{m_f}=0} = m_0 - [m_f]_{\boldsymbol{\rho},\lambda_{m_f}=0} = m_p + (\mathcal{M}_{m_p})_{\boldsymbol{\rho},\lambda_{m_f}=0}(\delta \boldsymbol{x}_0, \delta \boldsymbol{x}_f), \quad (5.19)$$

where m_p is the propellant mass consumed along the reference trajectory. Given any admissible interval set for $\delta \boldsymbol{x}_0$ and $\delta \boldsymbol{x}_f$, the polynomial bounder LDB is used to bound (5.19) and compute its range over the entire uncertainty set. Table 5.2 reports the resulting ranges for the 2-bang Earth–1996 FG_3 transfer under analysis, considering different error box amplitudes for the final target state. As expected, the reference propellent mass is inside the computed ranges. The propellent margins can be computed from the maximum and reference propellant masses. The results are reported in the same table.

Table 5.2: 2-bang Earth–1996 FG_3 transfer: propellant margins for the perturbed final spacecraft position test case.

Reference m_p: 186.318 kg		
Box amplitude [AU]	m_p range [kg]	Margin [%]
1E-5	[186.308, 186.329]	0.006
1E-4	[186.216, 186.421]	0.055
1E-3	[185.302, 187.354]	0.556

5.2.2 Perturbed initial spacecraft position

Similarly to the previous section, the case of perturbed initial spacecraft position is now analyzed. The vector $\boldsymbol{r}_0$ is supposed to be affected by measurable errors. Given any $\delta \boldsymbol{r}_0$, the polynomial map (5.15) is evaluated at $\delta \boldsymbol{x}_0 = [\delta \boldsymbol{r}_0, 0]$ and $\delta \boldsymbol{x}_f = [0, 0]$. That is, for any initial position error, the optimal values of $\boldsymbol{\lambda}_{x_0}$ and λ_{m_0} to reach the reference position of 1996 FG_3 at t_f from the perturbed initial position are computed. Moreover, map (5.16) is evaluated to identify the optimal control switching times of the new trajectory.

Table 5.1: Polynomial map of the final mass for the perturbed final spacecraft position test case.

Coefficient	Order	Exponents		
		$\delta r^*_{f,x}$	$\delta r^*_{f,y}$	$\delta r^*_{f,z}$
0.8757877896817668	0	0	0	0
-0.2900475782354168E-04	1	1	0	0
-0.2260461930716937E-04	1	0	1	0
0.1678135107041573E-04	1	0	0	1
-0.9864620265357797E-07	2	2	0	0
0.5598430126255891E-07	2	1	1	0
-0.1135468957957495E-07	2	0	2	0
-0.2220450919681012E-08	2	1	0	1
-0.8815529442612691E-08	2	0	1	1
-0.2082379629605812E-07	2	0	0	2
0.9932772407301452E-10	3	3	0	0
-0.8471790384760226E-10	3	2	1	0
0.2963836266557720E-10	3	1	2	0
-0.3861503491239163E-11	3	0	3	0
-0.2257098631676465E-10	3	2	0	1
-0.7115992598069297E-12	3	1	1	1
0.6693166032334217E-11	3	0	2	1
0.2387838098770029E-11	3	1	0	2
0.3595894845016061E-11	3	0	1	2
-0.1582726800632933E-10	3	0	0	3
0.2434732102635401E-13	4	4	0	0
-0.2670926104121093E-13	4	3	1	0
0.2991816209349861E-13	4	2	2	0
-0.1099850174875807E-13	4	1	3	0
0.9286659733380650E-15	4	0	4	0
0.2519160003801756E-13	4	3	0	1
0.3180325612380562E-13	4	2	1	1
-0.5014781758845476E-14	4	1	2	1
-0.1892596994259727E-14	4	0	3	1
0.2746315960228113E-13	4	2	0	2
-0.1411023005862691E-15	4	1	1	2
0.9858964743243934E-15	4	0	2	2
0.3130550949910231E-14	4	1	0	3
0.2518994206004270E-13	4	0	1	3
-0.2018029356772127E-14	4	0	0	4

As in the case of perturbed final position, a maximum error of 1E-3 AU is supposed to affect each component of the initial spacecraft position. The corners of the associated cube are sampled and the map (5.15) is evaluated

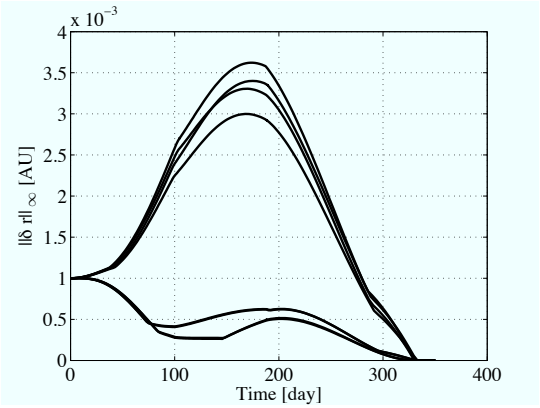

Figure 5.7: 2-bang Earth–1996 FG_3 transfer: optimal feedback on perturbed initial spacecraft positions. Trajectory displacement along the transfer.

for the optimal correction of the initial costates and control profiles. For each sample, the maximum norm between the resulting trajectories $\tilde{\boldsymbol{r}}(t)$ and the reference trajectory $\boldsymbol{r}(t)$ is reported in Figure 5.7. Starting from the initial error 1E-3 AU, the new trajectories approach the reference along the transfer and cancel the error at t_f.

Map (5.16) is again evaluated to obtain the optimal control switching times for the perturbed trajectories. The resulting Taylor polynomial in $\delta\boldsymbol{r}_0$ is reported in Table 5.3. More specifically, the fourth order Taylor approximation of the optimal variation of the first control switching time $[t_{s,1}]$ is illustrated. Similarly to Table 5.1, the Taylor polynomials are obtained in the scaled vector $\delta\boldsymbol{r}_0^* = \text{1E-4}\,\delta\boldsymbol{r}_0$.

Figure 5.8(a) plots the resulting optimal control magnitude profiles, whereas Figure 5.8(b) reports a detail on the resulting first control switch. The effect of the perturbed initial spacecraft positions on the control profiles is greater than in the case of perturbed final target positions, and the optimal switching time for the sampled trajectories varies within a range of about 8 days. The thrust components profiles corresponding to each sample are reported in Figure 5.9(a), whereas a detail of the first bang is reported in Figure 5.9(b).

The accuracy of the fourth order maps (5.15) and (5.16) is investigated by computing the final position error $\delta\boldsymbol{r}_f$ with respect to the target (refer to Figure 5.10(a) for an illustration of the defined quantities). The maximum norm over all the samples is reported in Figure 5.10(b) for different box amplitudes. The error increases with box amplitude. A comparison between Figure 5.10(b) and Figure 5.5(a) shows that the maps (5.15) and (5.16) are less accurate when used for the optimal feedback on the initial

Table 5.3: Polynomial map for the first control switching time of the perturbed initial spacecraft position test case.

Coefficient	Order	Exponents		
		$\delta r^*_{0,x}$	$\delta r^*_{0,y}$	$\delta r^*_{0,z}$
1.742641551394450	0	0	0	0
0.1035180131992654E-01	1	1	0	0
0.3713263031035156E-02	1	0	1	0
-0.1585227652931586E-03	1	0	0	1
0.1220688235269924E-04	2	2	0	0
-0.2363522270304565E-04	2	1	1	0
0.1190405319980039E-04	2	0	2	0
-0.5177378931475718E-06	2	1	0	1
0.1369045997044845E-06	2	0	1	1
0.1059739730644967E-05	2	0	0	2
-0.3929870277406426E-07	3	3	0	0
0.1173494821303832E-06	3	2	1	0
-0.1190718337781147E-06	3	1	2	0
0.4095160770173133E-07	3	0	3	0
-0.9824241735338258E-09	3	2	0	1
0.1113793805339660E-08	3	1	1	1
0.3028405935098672E-09	3	0	2	1
-0.1912165844074880E-08	3	1	0	2
0.2587986388725062E-08	3	0	1	2
0.7791564321805321E-10	3	0	0	3
0.1032437138481156E-09	4	4	0	0
-0.4369125667951222E-09	4	3	1	0
0.6871902593810353E-09	4	2	2	0
-0.4779345025238920E-09	4	1	3	0
0.1245662942951556E-09	4	0	4	0
0.1573071515439513E-10	4	3	0	1
-0.4230013379852996E-10	4	2	1	1
0.3799043635120375E-10	4	1	2	1
-0.1137245340920515E-10	4	0	3	1
0.1451578222696536E-11	4	2	0	2
-0.9389714160797251E-12	4	1	1	2
-0.2755045442037010E-11	4	0	2	2
0.2654869582923779E-11	4	1	0	3
-0.4832184593985633E-11	4	0	1	3
0.9083386633762300E-13	4	0	0	4

position. Nevertheless, similarly to the case of perturbed final position, the maps are sufficiently accurate to compute control corrections for error boxes of amplitude up to 1E-3 AU.

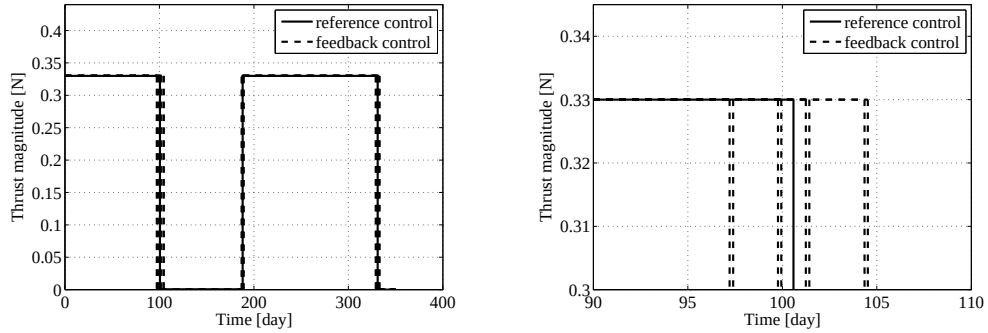

(a) Control profiles (b) Detail on first control switch

Figure 5.8: 2-bang Earth–1996 FG_3 transfer: optimal control profiles for perturbed initial spacecraft positions.

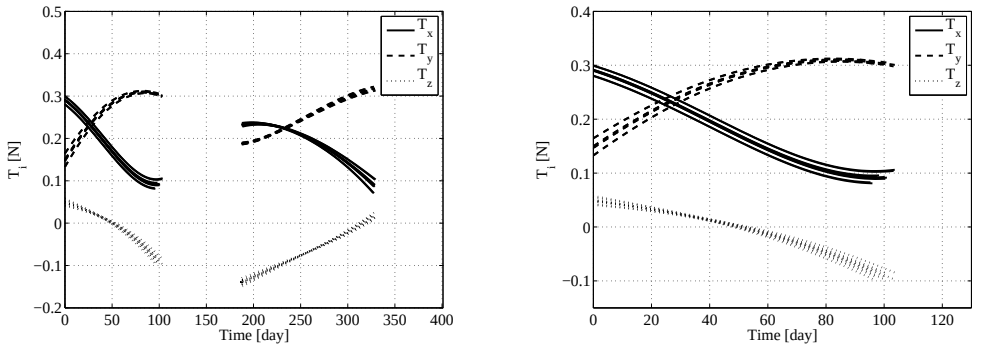

(a) Thrust components (b) Detail on first bang

Figure 5.9: 2-bang Earth–1996 FG_3 transfer: thrust components profiles for perturbed initial spacecraft positions.

Finally, similarly to the previous test case, the polynomial maps (5.18) and (5.19) are bounded for different error box amplitudes on the initial spacecraft position to compute propellant margins. The results are reported in Table 5.4.

5.3 Transfer to 1996 FG_3: 3-bang solution

The 3-bang reference trajectory to asteroid 1996 FG_3 (see Section 3.2.2) is now used as testbed for the algorithm. The fuel optimal transfer trajectory and control profile reported in Figures 3.2(a) and 3.2(c) are used as reference solution for the Taylor expansions. Fourth order maps (5.15) and

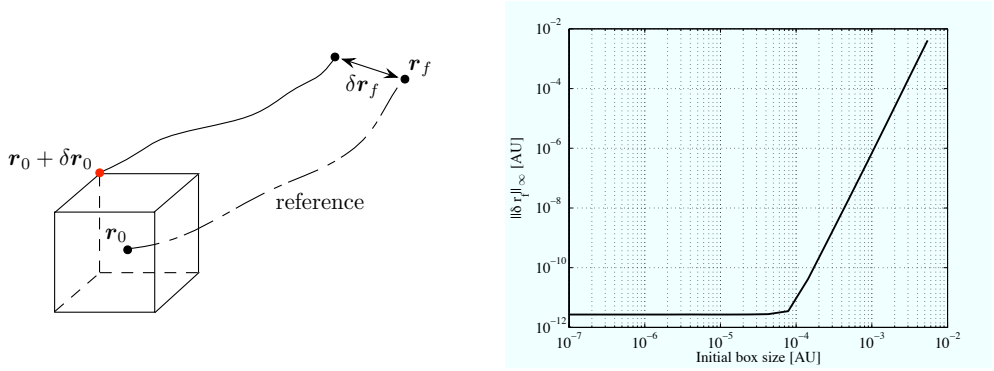

(a) Definition of the quantities for accuracy analysis

(b) Error vs. Box amplitude

Figure 5.10: 2-bang Earth–1996 FG_3 transfer: accuracy analysis for perturbed initial spacecraft positions.

Table 5.4: 2-bang Earth–1996 FG_3 transfer: propellant margins for the perturbed initial spacecraft position test case.

Reference m_p: 186.318 kg		
Box amplitude [AU]	m_p range [kg]	Margin [%]
1E-5	[186.297, 186.340]	0.012
1E-4	[186.106, 186.535]	0.117
1E-3	[184.347, 188.662]	1.258

(5.16) are computed using the algorithm introduced in Section 5.1. Similarly to the 2-bang solution, the cases of perturbed final and initial position are investigated.

5.3.1 Perturbed final target position

The final position of asteroid 1996 FG_3, $\boldsymbol{r}_f$, is supposed to be affected by measurable errors and the polynomial map (5.15) is evaluated by setting $\delta\boldsymbol{x}_0 \equiv [\delta\boldsymbol{r}_0, \delta\boldsymbol{v}_0] = [0, 0]$ and $\delta\boldsymbol{x}_f \equiv [\delta\boldsymbol{r}_f, \delta\boldsymbol{v}_f] = [\delta\boldsymbol{r}_f, 0]$ to obtain the optimal corrections to compensate the errors. The new values of the initial costates are computed and forward point-wise integrations of the ODEs (3.1) and (3.8) are performed to transfer the spacecraft from the reference initial state to the perturbed final target position.

First of all, a maximum perturbation of 1E-3 AU is supposed to affect each component of the final target position. For each corner of the corresponding cube, the associated error with respect to the reference final state is

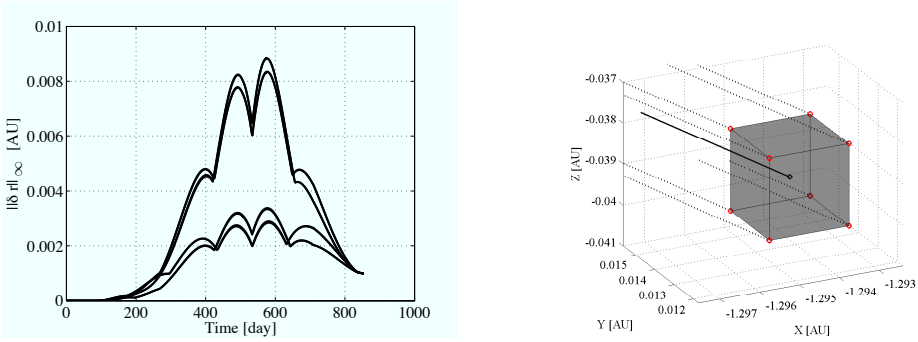

(a) Displacement along the transfer (b) Detail at arrival

Figure 5.11: 3-bang Earth–1996 FG_3 transfer: optimal feedback on perturbed final target positions.

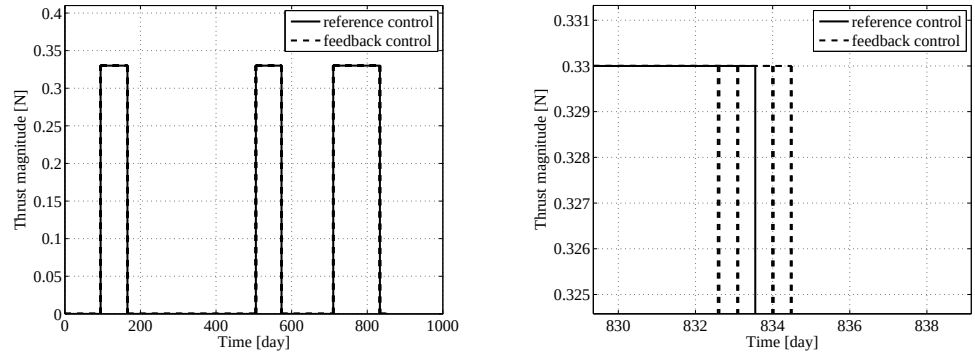

(a) Control profiles (b) Detail on last control switch

Figure 5.12: 3-bang Earth–1996 FG_3 transfer: optimal control profiles for perturbed final target positions.

computed and the map (5.15) is evaluated to obtain the new optimal transfer trajectory. Figure 5.11(a) plots the maximum norm of the difference between the resulting trajectory and the reference trajectory. The optimal feedback laws obtained with the fourth order corrections are able to guide the spacecraft from the reference initial state to the final imposed offset of 1E-3 AU. A detail of all trajectories at arrival is reported in Figure 5.11(b).

For each corner, map (5.16) is evaluated to obtain the optimal control switching times. Figure 5.12(a) plots the resulting optimal control magnitude profiles and Figure 5.12(b) reports a detail on the last control switch. Similarly to the 2-bang test case, the optimal switching time for the sampled trajectories varies within a range of about 2 days. For the sake of completeness, the feedback on the thrust direction is investigated in Figure 5.13(a).

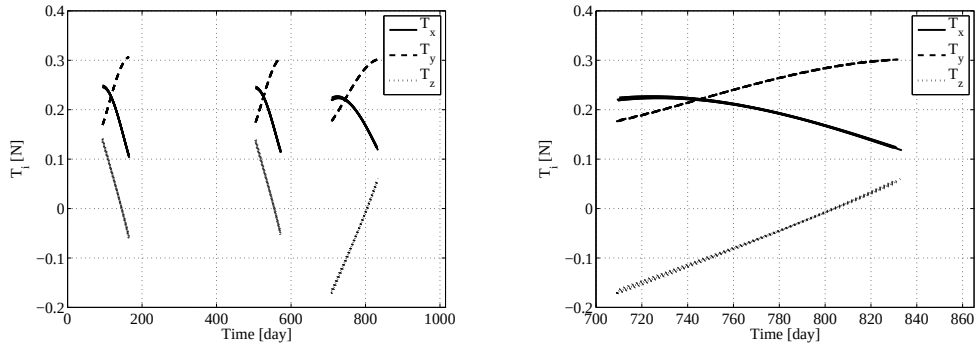

(a) Thrust components (b) Detail on last bang

Figure 5.13: 3-bang Earth–1996 FG_3 transfer: thrust components profiles for perturbed final target positions.

For each sample, the profiles of the components of the thrust vector are illustrated and a detail of the last bang is reported in Figure 5.13(b).

The accuracy of the high order feedback is now investigated. First of all, the effect of the amplitude of the perturbation is studied. Referring to Figure 5.4, for increasing box amplitudes, the difference $\delta\tilde{\boldsymbol{r}}_f$ between the final position and the imposed perturbed final target position is computed. The maximum norm for all samples is reported in Figure 5.14(a). As expected, the error increases with box amplitude. A comparison between Figure 5.14(a) and Figure 5.5(a) shows that the maximum error on the 3-bang reference trajectory is slightly greater than that achieved on the 2-bang case. Never-

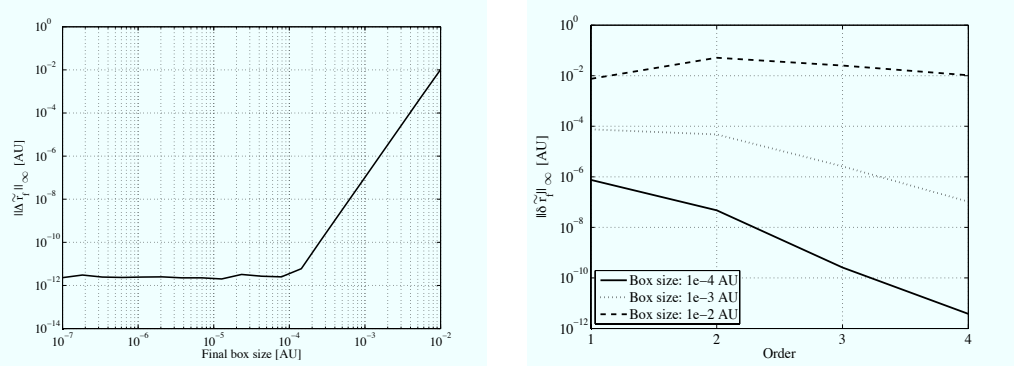

(a) Error vs. Box amplitude (b) Error vs. Order

Figure 5.14: 3-bang Earth–1996 FG_3 transfer: accuracy analysis for perturbed final target positions.

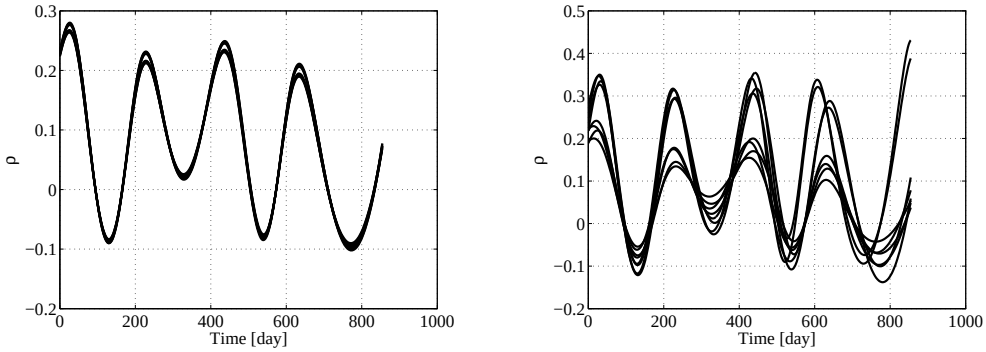

(a) Box amplitude: 10^{-3} AU (b) Box amplitude: 10^{-2} AU

Figure 5.15: 3-bang Earth–1996 FG_3 transfer: switching function for perturbed final target positions.

theless, the maps are still adequate to compute control corrections for boxes of amplitude up to 1E-3 AU, with a maximum error of about 1E-7 AU; i.e., four order of magnitude smaller than the perturbation.

Similarly to the 2-bang test case, Figure 5.15(a) and Figure 5.15(b) report the switching function profile for each sample and for box amplitudes of 1E-3 AU and 1E-2 AU, respectively. The figures confirm that the inaccuracy of the Taylor expansions for error boxes of amplitude larger than 1E-3 AU is mainly related to the breaking of the overall structure of the bang–bang control profile, which can not be handled by the Taylor expansion.

The improvement of the accuracy of the Taylor expansions for increasing order is studied in Figure 5.14(b). The trend of $\delta\tilde{\boldsymbol{r}}_f$ is reported in figure for increasing expansion orders and different error box amplitudes. Similarly to the 2-bang test case, the accuracy of the maps increases with order for box amplitudes up to 1E-3 AU. An irregular trend is confirmed for the amplitude of 1E-2 AU.

Finally, the polynomial maps (5.18) and (5.19) are computed for the 3-

Table 5.5: 3-bang Earth–1996 FG_3 transfer: propellant margins for the perturbed final spacecraft position test case.

Reference m_p: 200.884 kg		
Box amplitude [AU]	m_p range [kg]	Margin [%]
1E-5	[200.875, 200.893]	0.005
1E-4	[200.794, 200.975]	0.045
1E-3	[199.980, 201.795]	0.454

bang Earth–1996 FG_3 reference solution under analysis. Thus, the LDB polynomial bounder is used to compute the propellant margins for different error box amplitudes and the results are reported in Table 5.5.

5.3.2 Perturbed initial spacecraft position

The initial position is now supposed to be affected by measurable errors. For any error $\delta \boldsymbol{r}_0$, the polynomial map (5.15) is evaluated at $\delta \boldsymbol{x}_0 = [\delta \boldsymbol{r}_0, 0]$ and $\delta \boldsymbol{x}_f = [0, 0]$ to compute the optimal correction to the initial costates. The new values of $\boldsymbol{\lambda}_{x_0}$ and λ_{m_0} supplies the optimal control to reach the reference position of 1996 FG_3 at t_f from the perturbed initial position.

The performances of the algorithm are first assessed for a maximum error of 1E-3 AU on each component of the initial spacecraft position. The corners of the associated cube are sampled and the corresponding optimal transfers are computed by evaluating the map (5.15) and integrating the ODEs (3.1). Similarly to the previous test cases, for each sample, the maximum norm between the resulting trajectories and the reference trajectory is reported in Figure 5.16. The initial error of 1E-3 AU is reduced along the transfer and canceled at t_f.

The optimal control switching times are obtained by evaluating map (5.16). The resulting optimal control magnitude profiles and a detail on the first control switch are plotted in Figure 5.17(a) and Figure 5.17(b) respectively. Once again, the effect of perturbations on the initial spacecraft position is greater than for the case of perturbed final positions, and the optimal switching time for the sampled trajectories varies within a range of about 4 days. The thrust components profiles corresponding to each sample

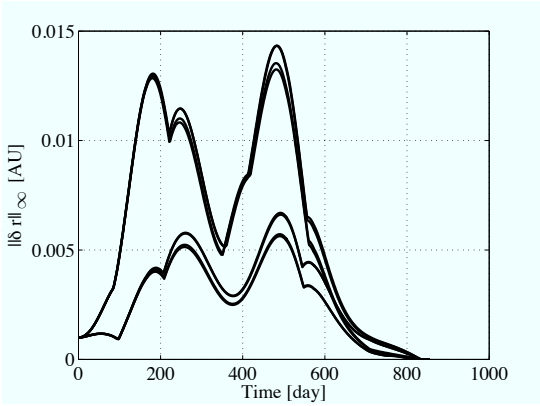

Figure 5.16: 3-bang Earth–1996 FG_3 transfer: optimal feedback on perturbed initial spacecraft positions. Trajectory displacement along the transfer.

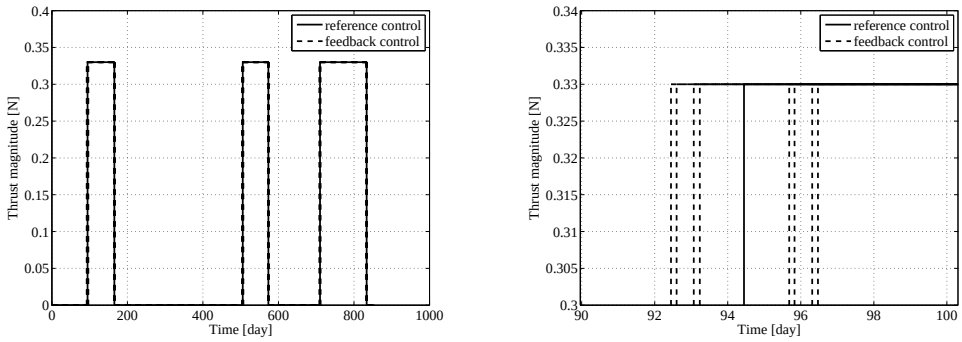

(a) Control profiles (b) Detail on first control switch

Figure 5.17: 3-bang Earth–1996 FG_3 transfer: optimal control profiles for perturbed initial spacecraft positions.

are reported in Figure 5.18(a), whereas a detail of the first bang is reported in Figure 5.18(b).

The accuracy of the fourth order maps (5.15) and (5.16) is investigated by computing the final position error $\delta \boldsymbol{r}_f$ with respect to the target. The maximum norm over all the samples for different box amplitudes is reported in Figure 5.19. The error increases with box amplitude. The results are comparable with those achieved for the 2-bang test case: the maps are sufficiently accurate to compute control corrections for error boxes of amplitude up to 1E-3 AU.

Similarly to the previous test cases, the polynomial maps (5.18) and (5.19)

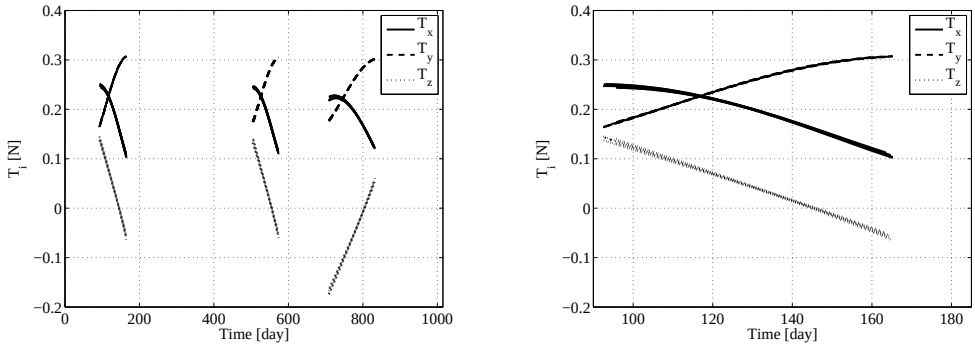

(a) Thrust components (b) Detail on first bang

Figure 5.18: 3-bang Earth–1996 FG_3 transfer: thrust components profiles for perturbed initial spacecraft positions.

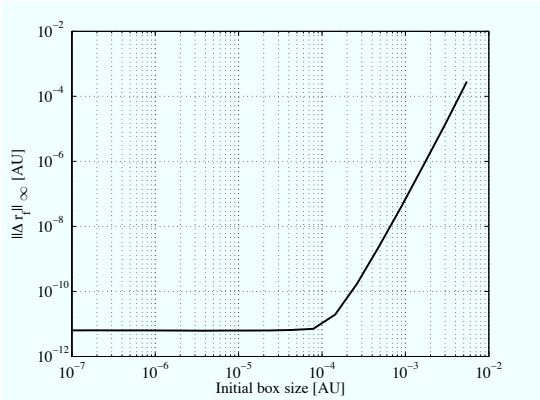

Figure 5.19: 3-bang Earth–1996 FG_3 transfer. Accuracy analysis for perturbed initial spacecraft positions: error vs. box amplitude

of the 3-bang transfer are bounded for different error box amplitudes on the initial spacecraft position to compute propellant margins. The results are reported in Table 5.6.

Table 5.6: 3-bang Earth–1996 FG_3 transfer: propellant margins for the perturbed initial spacecraft position test case.

Reference m_p: 200.884 kg		
Box amplitude [AU]	m_p range [kg]	Margin [%]
1E-5	[200.874, 200.894]	0.005
1E-4	[200.783, 200.985]	0.050
1E-3	[199.891, 201.910]	0.510

5.4 Transfer to 1996 FG_3: 4-bang solution

The 4-bang trajectory to asteroid 1996 FG_3 reported in Section 3.2.3 is now used as reference solution. Fourth order maps (5.15) and (5.16) are computed using the algorithm introduced in Section 5.1. The performances of the method are studied hereafter on perturbed final and initial positions.

5.4.1 Perturbed final target position

The case of measurable errors on the final position of asteroid 1996 FG_3 is addressed in this section. Given any final position error $\delta \boldsymbol{r}_f$, the polynomial

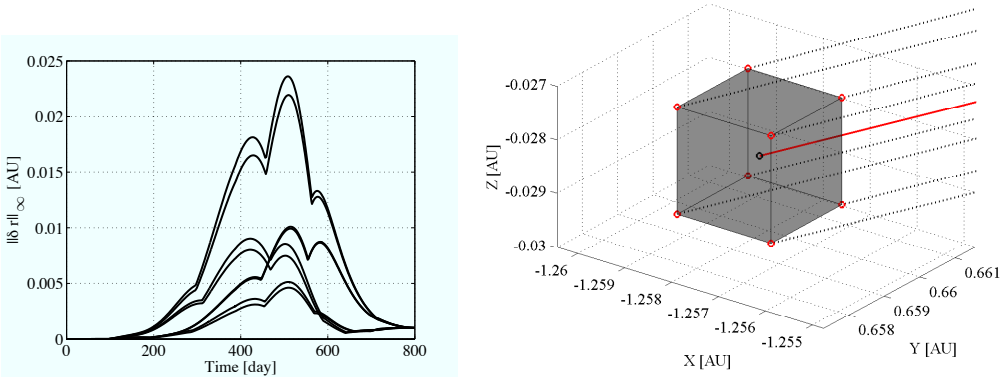

(a) Displacement along the transfer

(b) Detail at arrival

Figure 5.20: 4-bang Earth–1996 FG_3 transfer: optimal feedback on perturbed final target positions.

map (5.15) is evaluated by setting $\delta\boldsymbol{x}_0 \equiv [\delta\boldsymbol{r}_0, \delta\boldsymbol{v}_0] = [0, 0]$ and $\delta\boldsymbol{x}_f \equiv [\delta\boldsymbol{r}_f, \delta\boldsymbol{v}_f] = [\delta\boldsymbol{r}_f, 0]$. The new optimal values of the initial costates are then computed, which deliver the optimal control corrections to transfer the spacecraft from the reference initial state to the perturbed final target position.

The case of a maximum perturbation of 1E-3 AU on each component of the final target position is first investigated. For each corner of the corresponding cube, the associated $\delta\boldsymbol{r}_f$ is computed and the map (5.15) is evaluated to obtain the new optimal transfer trajectory. The resulting maximum norm of the difference between the resulting trajectory and the reference trajectory is reported in Figure 5.20(a). Similarly to the previous test cases, the fourth order corrections guide the spacecraft from the reference initial state to the final imposed offset of 1E-3 AU. A detail of all trajectories at arrival is reported in Figure 5.20(b).

The effect of the errors on the control switching times is instigated by evaluating map (5.16) for each corner of the error box. Figure 5.21(a) plots the resulting optimal control magnitude profiles and Figure 5.21(b) reports a detail at the end of the first bang, which shows the largest variation on the switching time. Compared to the 2-bang and 3-bang test cases, the 4-bang solution is characterized by larger ranges for the switching times, reaching a maximum of about 4 days. For the sake of completeness, the feedback on the thrust direction is investigated in Figure 5.22(a). The profiles of the components of the thrust vector are illustrated and a detail of the first bang is reported in Figure 5.22(b).

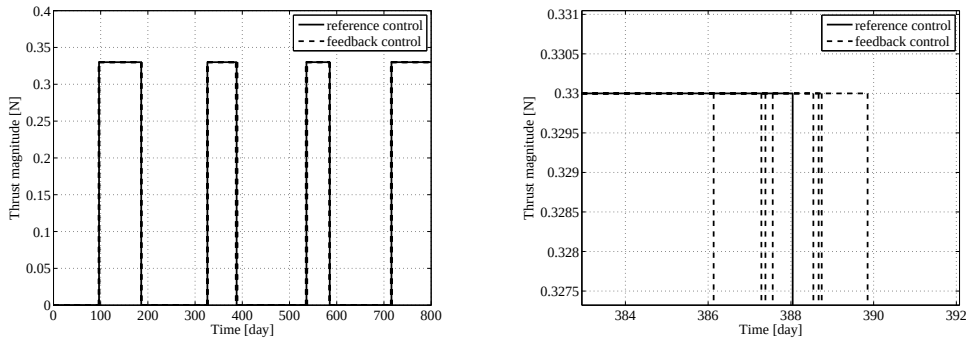

(a) Control profiles (b) Detail on last control switch

Figure 5.21: 4-bang Earth–1996 FG_3 transfer: optimal control profiles for perturbed final target positions.

The performances of the method for different error box amplitudes are studied in Figure 5.23(a). More specifically, referring again to Figure 5.4, for increasing box amplitudes, the difference $\delta\tilde{\boldsymbol{r}}_f$ between the final position and the imposed perturbed final target position is computed. The maximum norm for all samples is reported in the figure. By comparing Figure 5.23(a) with Figure 5.14(a) and Figure 5.5(a), we can see that the maximum error for the 4-bang is evidently greater than those achieved in the 2-bang and 3-bang cases, especially for larger box amplitudes. In particular, the maximum error for a box amplitude of 1E-3 AU is about 1E-5 AU; i.e., two orders of magnitude greater than in the other test cases. Nevertheless, it is still

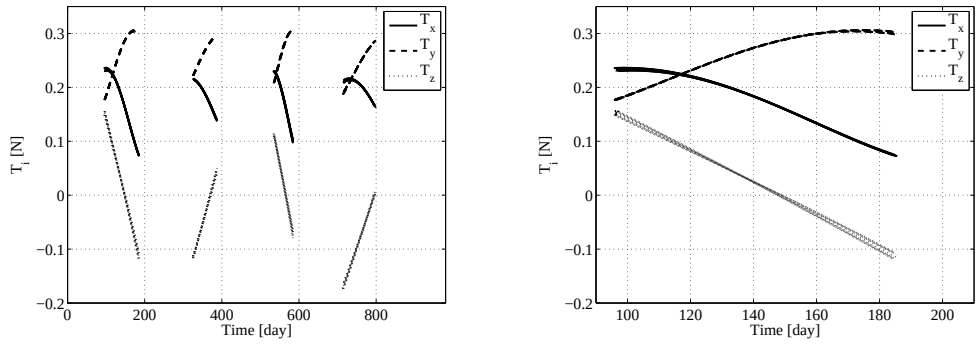

(a) Thrust components (b) Detail on first bang

Figure 5.22: 4-bang Earth–1996 FG_3 transfer: thrust components profiles for perturbed final target positions.

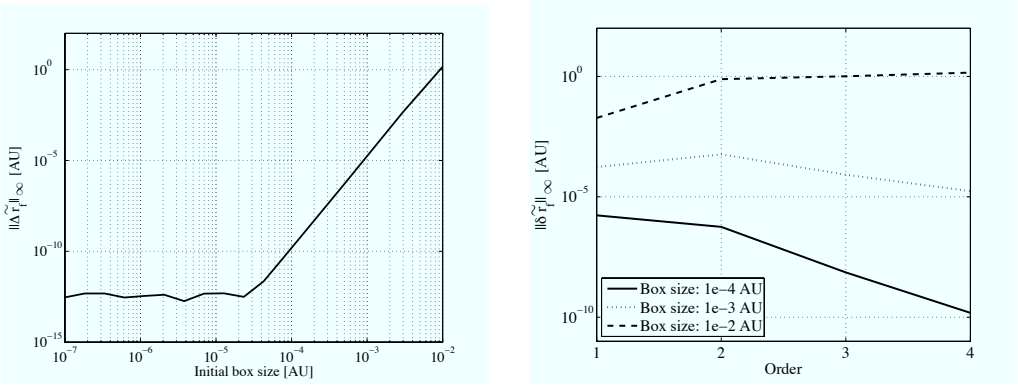

(a) Error vs. Box amplitude (b) Error vs. Order

Figure 5.23: 4-bang Earth–1996 FG_3 transfer: accuracy analysis for perturbed final target positions.

limited to 1% of the imposed perturbation. For the sake of completeness, the switching function profile for each sample and for box amplitudes of 1E-3 AU and 1E-2 AU are studied in Figure 5.24(a) and Figure 5.24(b), respectively. The figures confirm the rationales of the inaccuracy of the Taylor expansions for error boxes of amplitude larger than 1E-3 AU.

The incipient inaccuracy of the Taylor expansions for error boxes larger than 1E-4 AU is confirmed instead by the trend of the maximum error for increasing expansion orders reported in Figure 5.23(b). More specifically, the accuracy of the maps still increases with order for box amplitudes up to 1E-4 AU. However, unlike the 2-bang and 3-bang test cases, an irregular trend

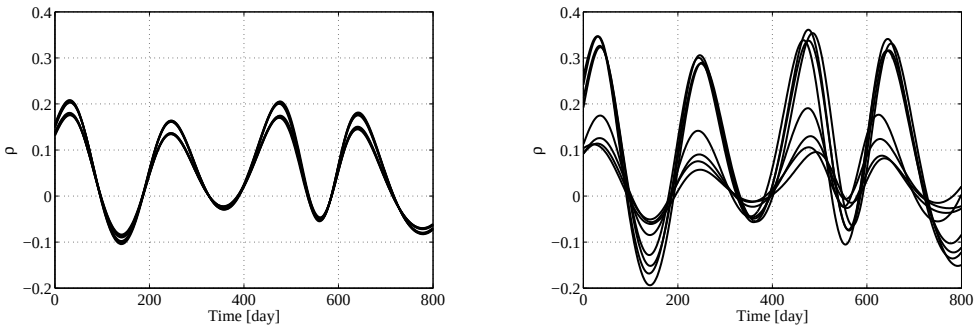

(a) Box amplitude: 10^{-3} AU (b) Box amplitude: 10^{-2} AU

Figure 5.24: 4-bang Earth–1996 FG_3 transfer: switching function for perturbed final target positions.

appears for the 1E-3 AU.

Finally, the propellant margins are assessed by computing the polynomial maps (5.18) and (5.19) for the 4-bang Earth–1996 FG_3 reference solution under analysis. The LDB polynomial bounder is used to bound the resulting maps for different error box amplitudes. The results are reported in Table 5.7.

Table 5.7: 4-bang Earth–1996 FG_3 transfer: propellant margins for the perturbed final spacecraft position test case.

Reference m_p: 217.828 kg		
Box amplitude [AU]	m_p range [kg]	Margin [%]
1E-5	[217.820, 217.836]	0.004
1E-4	[217.749, 217.908]	0.037
1E-3	[217.038, 218.632]	0.369

5.4.2 Perturbed initial spacecraft position

The case of perturbed initial position is studied in this section. For any error $\delta \boldsymbol{r}_0$, the polynomial map (5.15) is evaluated at $\delta \boldsymbol{x}_0 = [\delta \boldsymbol{r}_0, 0]$ and $\delta \boldsymbol{x}_f = [0, 0]$. The associated values of $\boldsymbol{\lambda}_{x_0}$ and λ_{m_0} supplies the optimal control to reach the reference position of 1996 FG_3 at t_f from the perturbed initial position.

A maximum perturbation of 1E-3 AU is set on each component of the initial spacecraft position to study feedback performances. The corners of the associated cube are sampled and the corresponding optimal transfers are

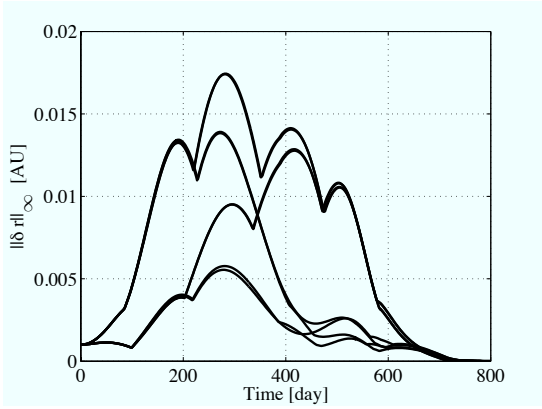

Figure 5.25: 4-bang Earth–1996 FG_3 transfer: optimal feedback on perturbed initial spacecraft positions. Trajectory displacement along the transfer.

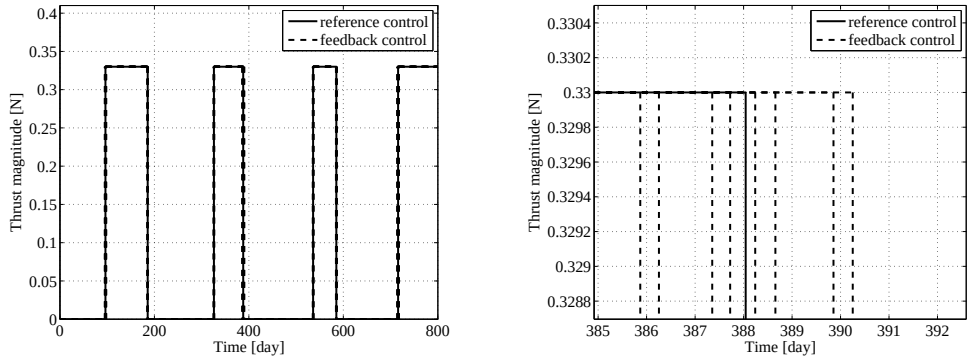

(a) Control profiles (b) Detail on first control switch

Figure 5.26: 4-bang Earth–1996 FG_3 transfer: optimal control profiles for perturbed initial spacecraft positions.

computed by evaluating the map (5.15). Figure 5.25 reports the profiles of the position displacement with respect to the reference trajectory for each corner of the initial error box. Similarly to the other test cases, the displacement is supplied in terms of the maximum norm between the resulting trajectories and the reference trajectory. The initial error of 1E-3 AU is reduced along the transfer and canceled at t_f.

The associated variation of the optimal control switching times is illustrated in Figure 5.26(a). A detail of the switch at the end of the second bang is reported in Figure 5.26(b), which shows that the maximum variation of the switching times is of the order of 4 days. The thrust components profiles

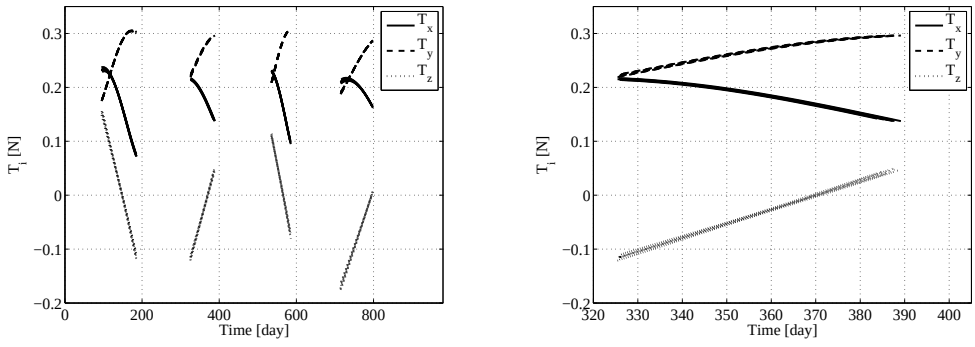

(a) Thrust components (b) Detail on second bang

Figure 5.27: 4-bang Earth–1996 FG_3 transfer: thrust components profiles for perturbed initial spacecraft positions.

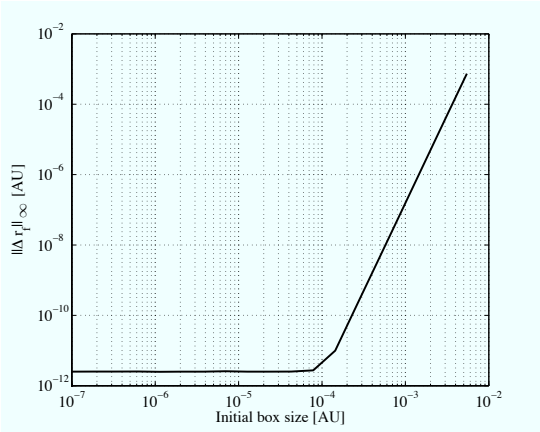

Figure 5.28: 4-bang Earth–1996 FG_3 transfer. Accuracy analysis for perturbed initial spacecraft positions: error vs. box amplitude

corresponding to each sample are reported in Figure 5.27(a), whereas a detail of the second bang is reported in Figure 5.27(b).

The trend of the error of the fourth order Taylor expansion for different box amplitudes is investigated in Figure 5.28. More specifically, the maximum norm of the final position error with respect to the target over all the samples, $\|\delta \boldsymbol{r}_f\|_\infty$, is plotted. Unlike the perturbed final position test case, the results show that the accuracy of the Taylor expansions for the 4-bang solution do not drop significantly with respect to the 2-bang and 3-bang cases: the maps are sufficiently accurate to compute control corrections for error boxes of amplitude up to 1E-3 AU.

Similarly to the previous test cases, the polynomial maps (5.18) and (5.19) of the 4-bang transfer are bounded for different error box amplitudes on the initial spacecraft position to compute propellant margins. The results are reported in Table 5.8.

Table 5.8: 4-bang Earth–1996 FG_3 transfer: propellant margins for the perturbed initial spacecraft position test case.

Reference m_p: 217.828 kg		
Box amplitude [AU]	m_p range [kg]	Margin [%]
1E-5	[217.817, 217.839]	0.005
1E-4	[217.719, 217.938]	0.051
1E-3	[216.749, 218.941]	0.511

Chapter 6

Conclusions

The work addressed the development of high order methods to manage optimal control problems with uncertain boundary conditions, including the constraint of control saturation. More specifically, the study focused on the design of continuously-propelled fuel-optimal trajectories, with applications to the transfer to asteroid 1996 FG_3. The this aim, three major areas were covered:

- the identification of a reference transfer trajectory, i.e., a reference solution of the fuel-optimal control problem;
- the development of an algorithm for the high order expansion of an approximate smooth solution of the fuel-optimal problem, with respect to both the initial spacecraft state and final target state;
- the development of an algorithm for the high order expansion of the exact bang-bang solution of the fuel-optimal problem, with respect to both the initial spacecraft state and final target state.

A smoothing method was applied to obtain a reference solution of the fuel-optimal Earth–1996 FG_3 transfer problem. More specifically, the solution of the associated minimum-energy optimal control problem is first computed. Then, a $\mathcal{C}^\infty$ approximation of the discontinuous solution of the fuel-optimal problem is set up, with the explicit dependence on a continuation parameter p, which can be varied to better approximate the bang–bang solution. A sequence of optimal control problems is then solved by continuing on p, until a sufficiently accurate solution of the discontinuous problem is obtained. This is used as first guess for the solution of the exact fuel-optimal problem. The method showed good flexibility and robustness, and allowed the computation of reference trajectories for relatively long transfer times and increasing number of switches.

With reference to the solution process described above, a method for the high order expansion of the approximate solution of the fuel-optimal problem was first developed. More specifically, the outcome of the continuation process (i.e., the last $\mathcal{C}^\infty$ approximation of the bang–bang solution) is taken as reference trajectory. Then, differential algebra is used to expand the approximate solution with respect to both the initial spacecraft state and the final target state. For any perturbed initial and final state, the new optimal control laws are obtained by the evaluation of the resulting polynomials. This guarantees sufficient accuracy in nonlinear dynamics, reducing at the same time the computational burden of classical nonlinear methods.

The $\mathcal{C}^\infty$ nature of the solutions obtained with the above method enables an easier management of the Taylor expansions. Nevertheless, the method supplies only approximate solutions of the original problem. Thus, a DA-based algorithm for the Taylor expansion of the exact bang-bang solution was developed. To this aim, the integration over the entire reference trajectory is subdivided in its bang–bang branches. Then, differential algebra is used to obtain the high order expansion of the initial costates and the optimal switching times with respect to the initial and final conditions. Thus, the method improves the results of classical techniques based on the linearization of the dynamics. Moreover, it reduces the computation of the optimal thrust direction and switching times along the transfer to the evaluation of polynomials, which is a valuable advantage over the conventional nonlinear optimal control strategies that are mainly based on iterative procedures. The main limitation of the method is that it is intrinsically valid for the bang-bang structure of the reference trajectory. Thus, the Taylor expansions are not able to handle the appearance or disappearance of control switches in the optimal solution for perturbed initial and final states.

Both methods have shown good performances in terms of control accuracy for a large uncertainty set on both the initial spacecraft position and the final target position. More specifically, for the Earth–1996 FG_3 transfer solutions analyzed in this study, the methods are able to compensate for a maximum error of 1E-3 AU, which is well above the errors to be managed in practical applications. For larger error boxes, the accuracy of the Taylor expansions drops off rapidly. This was shown to be related to the appearance of additional switches in the control law.

Among the main advantages of differential algebra, the possibility of computing propellant margins was investigated. To this aim, the polynomial map of the consumed propellant was computed and the polynomial bounder LDB was used to assess its range over the admissible uncertainty sets. This enabled an easy and immediate computation of the margins.

Future work will be aimed at addressing the imposition of soft boundary constraints, as well as at the minimization of alternative performance criteria. In addition, the methods will be applied to additional test problems and a strategy for its onboard implementation will be developed. This will contribute to a comprehensive identification of its potentialities and limits in space-related applications.

Bibliography

[1] R. Armellin, P. Di Lizia, F. Bernelli-Zazzera, M. Berz, Asteroid Close Encounters Characterization using Differential Algebra: The Case of Apophis, Celestial Mechanics and Dynamical Astronomy, Vol. 107, pp. 451–472, 2010.

[2] R. Armellin, F. Topputo, A Sixth-Order Accurate Scheme for Solving Two-Point Boundary Value Problems in Astrodynamics, Celestial Mechanics and Dynamical Astronomy, Vol. 96, pp. 289-309, 2006.

[3] S.C. Beeler, State-dependent Riccati Equation Regulation of Systems with State and Control Nonlinearities, NIA Report No. 2004-08, National Institute of Aerospace, Hampton, Virginia, 2004.

[4] F. Bernelli-Zazzera, M. Vasile, M. Massari, P. Di Lizia, Assessing the accuracy of interval arithmetic estimates in space flight mechanics, Final Report, Contract No. 18851/05/NL/MV, 2004.

[5] F. Bernelli-Zazzera, M. Berz, M. Lavagna, K. Makino, R. Armellin, P. Di Lizia, R. Jagasia, F. Topputo, NEO Encounter 2029: Orbital Prediction via Differential Algebra and Taylor Models, FInal Report, Contract No. 20271/06/NL/HI, 2009.

[6] M. Berz, Modern Map Methods in Particle Beam Physics, Academic Press, 1999.

[7] M. Berz, The new method of TPSA algebra for the description of beam dynamics to high orders, Technical Report AT-6:ATN-86-16, Los Alamos National Laboratory, 1986.

[8] M. Berz, The method of power series tracking for the mathematical description of beam dynamics, Nuclear Instruments and Methods A258, 431, 1987.

[9] M. Berz, High-Order Computation and Normal Form Analysis of Repetitive Systems, Physics of Particle Accelerators, Vol. AIP 249, 456, 1991.

[10] M. Berz, K. Makino, Y. Kim, Long-term stability of the tevatron by verified global optimisation, Nuclear Instruments and Methods, A558, pp. 1–10, 2005.

[11] M. Berz, K. Makino, COSY Infinity version 9 reference manual, MSU Report MSUHEP-060803, Michigan State University, East Lansing, MI 48824, 2006.

[12] B. Bonnard, J.B. Caillau, Introduction to nonlinear optimal control, in Advanced topics in control systems theory, Lecture Notes in Control and Inform. Sci., Springer, 2006.

[13] A. Bryson, Y. Ho, Applied Optimal Control: optimization, estimation, and control, Hemisphere Publishing Co.s, Washigton, 1975.

[14] T. Bullock, G. Franklin, A second-order feedback method for optimal control computations, IEEE Transactions on Automatic Control, Vol. 12, pp. 666–673, 1967.

[15] T. Cimen, Survey of State-Dependent Riccati Equation in Nonlinear Optimal Feedback Control Synthesis, Journal of Guidance, Control, and Dynamics, Vol. 35, pp. 1025–1047, 2012.

[16] J. Cloutier, C. D'Souza, C. Mracek, Nonlinear Regulation and Nonlinear H_∞ Control via the State-dependent Riccati Equation Technique; Part 1, theory; Part 2, examples, Proceedings of the First International Conference on Nonlinear Problems in Aviation and Aerospace, pp. 117–141, 1996.

[17] L.G. Crespo, J.Q. Sun, Stochastic Optimal Control via Bellmans Principle, NASA/CR-2003-212419, 2003.

[18] G. Dahlquist, A. Bjorck, Numerical Methods, Series in computational methods in mechanics and thermal sciences, Prentice-Hall, 1974.

[19] P. Di Lizia, Robust Space Trajectory and Space System Design Using Differential Algebra, PhD Thesis, Politecnico di Milano, 2008.

[20] P. Di Lizia, R. Armellin, A. Ercoli-Finzi, M. Berz, High-Order Robust guidance of Interplanetary Trajectories based on Differential Algebra,

Journal of Aerospace Engineering, Sciences and Applications, Vol. 1, pp. 43–57, 2008.

[21] P. Di Lizia, R. Armellin, and M. Lavagna, Application of high order expansions of two-point boundary value problems to astrodynamics, Celestial Mechanics and Dynamical Astronomy, Vol. 102, pp. 355–375, 2008.

[22] P. Di Lizia, R. Armellin, F. Bernelli-Zazzera, M. Berz, High Order Optimal Feedback Control of Lunar Landing and Rendezvous Trajectoriesl, Proceedings of the 3rd CEAS Air & Space Conference and XXI Congresso Nazionale AIDAA, pp. 1221–1230, 2011.

[23] G. Fusai, Implementing Models in Quantitative Finance: Methods and Cases, Springer, 2008.

[24] F. Jiang, H. Baoyin, J. Li, Practical Techniques for Low-Thrust Trajectory Optimization with Homotopic Approachs, Journal of Guidance, Control, and Dynamics, Vo. 35, pp. 245–258, 2012.

[25] F.J. Gil-Fernandez, M. Graziano, M.A. Gomez-Tierno, E. Milic, Autonomous Low-Thrust Guidance: Application to SMART-1 and Bepi-Colombo. Annals of the New York Academy of Sciences, pp. 307–327, 2004.

[26] D. F. Lawden, Optimal Trajectories for Space Navigation, Butterworths, London, 1963.

[27] K. Makino, Rigorous Analysis of Nonlinear Motion in Particle Accelerators, Ph.D. Thesis, Michigan State University, East Lansing, Michigan, USA, 1998.

[28] K. Makino, M. Berz, Verified Global Optimization with Taylor Model-based Range Bounders, Transactions on Computers, 11, pp. 1611–1618, 2005.

[29] R.E. Moore, Interval Analysis, Prentice Hall, Englewood Cliffs, NJ, 1966.

[30] C.P. Mracek, J.R. Cloutier, Control designs for the nonlinear benchmark problem via the state-dependent Riccati equation method, International Journal of Robust and Nonlinear Control, Vol. 8, pp. 401–433, 1998.

[31] J.T. Olympio, Algorithm for low thrust optimal interplanetary transfers with escape and capture phases, AIAA/AAS Astrodynamics Specialist Conference and Exhibit, Honolulu, Hawaii, August 2008.

[32] C. Park, D. Scheeres, Extended Applications of Generating Functions to Optimal Feedback Control Problems, Proceedings of the American Control Conference, 2005.

[33] C. Park, D. Scheeres, Solution of Optimal Feedback Control Problems with General Boundary Conditions Using Hamiltonian Dynamics and Generating Functions, Automatica, Vol. 42, pp. 869–875, 2006.

[34] J.D. Pearson, Approximation methods in optimal control, Journal of Electronics and Control, Vol. 13, pp. 453–469, 1962.

[35] V. Rico-Ramirez, U. M. Diwekar, Stochastic Maximum Principle for Optimal Control under uncertainty, Computers and Chemical Engineering, 28, 2845-2849, 2004.

[36] C.A. Renault, D.J. Scheeres, Statistical Analysis of Control Maneuvers in Unstable Orbital Environments, Journal of Guidance, Control, and Dynamics, Vol. 26, pp. 758–769, 2003.

[37] A. Wernli, G. Cook, Suboptimal control for the nonlinear quadratic regulator problem, Automatica, Vol. 11, pp. 75–84, 1975.

[38] M. Xin, S.N. Balakrishnan, D.T. Stansbery, E.J. Ohlmeyer, Nonlinear Missile Autopilot Design with $\theta - D$ Technique, Journal of Guidance, Control and Dynamics, Vol. 27, pp. 406–417, 2004.

[39] Space Trajectory Optimisation under Uncertainties (Ref: 10-4101), Annex B. 2010/01 Call for Proposals: Study descriptions.